Upconversion Detection for Improved Nonlinear Mid-infrared Spectroscopy in Flames

Lyngbye Pedersen, Rasmus

2019

Document Version:
Publisher's PDF, also known as Version of record

Link to publication

Citation for published version (APA):
Lyngbye Pedersen, R. (2019). *Upconversion Detection for Improved Nonlinear Mid-infrared Spectroscopy in Flames*. Department of Physics, Lund University.

Total number of authors:
1

Upconversion Detection for Improved Nonlinear Mid-infrared Spectroscopy in Flames

RASMUS L. PEDERSEN

DEPARTMENT OF PHYSICS | FACULTY OF ENGINEERING | LUND UNIVERSITY

Printed by Media-Tryck, Lund 2019 NORDIC SWAN ECOLABEL 3041 0903

LUND
UNIVERSITY

Faculty of Engineering
Department of Physics
Lund University

Lund Reports on Combustion Physics, LRCP-219
ISBN 978-91-7895-249-6
ISSN 1102-8718
ISRN LUTFD2/TFCP-219-SE

9 789178 952496

Upconversion Detection for Improved Nonlinear Mid-infrared Spectroscopy in Flames

Upconversion Detection for Improved Nonlinear Mid-infrared Spectroscopy in Flames

by Rasmus L. Pedersen

DOCTORAL DISSERTATION
Thesis advisors: Dr. Zhongshan Li, Dr. Peter Tidemand-Lichtenberg
Faculty opponent: Professor Juha Toivonen

To be presented, with the permission of the Faculty of Engineering of Lund University, for public criticism at Hall K404, at the Department of Physics on Tuesday, the 17th of December 2019 at 9:15.

Organization
LUND UNIVERSITY

Department of Physics
Box 118
SE–221 00 LUND
Sweden

Document name
DOCTORAL DISSERTATION

Date of disputation
2019-12-17

Sponsoring organization

Author(s)
Rasmus L. Pedersen

Title
Upconversion Detection for Improved Nonlinear Mid-infrared Spectroscopy in Flames

Abstract

This thesis deals with the addition of upconversion detection to non-linear mid-infrared laser spectroscopy techniques. The techniques investigated here are degenerate four wave mixing (DFWM) and infrared polarization spectroscopy (IRPS). These techniques are useful for detecting many of the key species in combustion, such as CH_4, C_2H_6, HCl, and HCN. These species can be probed using ro-vibrational transitions in the mid-infrared, but lack transition that would make detection possible in the visible or near-infrared. These techniques allow spatially resolved, non intrusive and sensitive detection of these important species directly in flames.

The main focus has been on investigating the new opportunities that upconversion detection makes possible. It had already been demonstrated that upconversion greatly improved the sensitivity of DFWM. As a part of this thesis work, it was shown that signal to noise ratio of IRPS was also improved by upconversion, although not to the same degree.

DFWM with upconversion was used to quantitatively measure HCN released during the devolatilization phase of burning straw pellets, which was only possible due to the improved sensitivity of the detection system. A major part of quantifying concentration measurements is achieving accurate temperature measurements, as the signal scales with temperature. A method of measuring temperature using the relative strength of transition lines of water had been described before this thesis. The effects of signal saturation for waterline thermometry were investigated as part of this thesis to increase the precision and reliability of temperature measurements, as this would aid in achieving more accurate concentration measurements.

Key words
Upconversion, Infrared, HCN, Thermometry, Degenerate four wave mixing, polarization spectroscopy

Classification system and/or index terms (if any)

Supplementary bibliographical information

Language
English

ISSN and key title

ISBN
978-91-7895-249-6 (print)
978-91-7895-250-2 (pdf)

Recipient's notes

Number of pages
144

Price

Security classification

I, the undersigned, being the copyright owner of the abstract of the above-mentioned dissertation, hereby grant to all reference sources the permission to publish and disseminate the abstract of the above-mentioned dissertation.

Signature

Date 2019-11-06

Upconversion Detection for Improved Nonlinear Mid-infrared Spectroscopy in Flames

by Rasmus L. Pedersen

LUND
UNIVERSITY

Funding information: Mid-TECH (H2020-MSCAITN-2014, 642661),

Faculty of Engineering, Department of Physics

ISBN: 978-91-7895-249-6 (print)
ISBN: 978-91-7895-250-2 (pdf)

Printed in Sweden by Media-Tryck, Lund University, Lund 2019

Contents

List of publications iii
Acknowledgements iv
Populærvidenskabelig Sammenfatning v

Definitions and Abbreviations **1**
0.1 Definitions 1
0.2 Abbreviations 4

1 Introduction **5**

2 Flame and Burner **9**

3 Molecular Spectroscopy **13**
3.1 HITRAN: Calculating Linestrength and Shape 15
3.2 Measuring Laser-Linewidths 19

4 Nonlinear Optics **21**
4.1 2nd Order Effects 21
4.2 Sum Frequency Generation 21
4.3 Difference Frequency Generation 25
4.4 3rd Order Effects 26
4.5 IRPS 27
4.6 DFWM 31
4.7 Thermometry 37
4.8 Waterline Thermometry 38

5 Upconversion **45**
5.1 Upconversion Detector 48

6 Noise **51**
6.1 Reference Beam for IRPS 52

7 Lasers **57**
7.1 Introduction 57
7.2 Quantum Cascade Lasers 57
7.3 Dye Laser System 59

7.4 Optical Parametric Generator 61

8 Summary and Perspective 67

8.1 Main results of the research papers 68

8.2 References 69

Scientific publications 83

Author contributions 83

Paper I: Mid-Infrared Polarization Spectroscopy Measurements of Species Concentrations and Temperature in a Low-Pressure Flame . 85

Paper II: Comparison of an InSb Detector and Upconversion Detector for Infrared Polarization Spectroscopy 99

Paper III: Spatially and temporally resolved IR-DFWM measurement of HCN released from gasification of biomass pellets 107

Paper IV: Infrared Degenerate Four-wave Mixing with Upconversion Detection for Quantitative Gas Sensing 117

Paper V: Characterization of the NEP of Mid-Infrared Upconversion Detectors 127

List of publications

This thesis is based on the following publications, referred to by their Roman numerals:

I **Mid-Infrared Polarization Spectroscopy Measurements of Species Concentrations and Temperature in a Low-Pressure Flame**
A. Sahlberg, D. Hot, **R. Pedersen**, J. Zhou, M. Aldén, and Z. Li.
Applied Spectroscopy, 2019, Vol. 73, p. 1–12

II **Comparison of an InSb Detector and Upconversion Detector for Infrared Polarization Spectroscopy**
R. Pedersen, D. Hot, and Z. Li.
Applied Spectroscopy, 2018, Vol. 72, p. 793–797

III **Spatially and temporally resolved IR-DFWM measurement of HCN released from gasification of biomass pellets**
D. Hot, **R. Pedersen**, W. Weng, Y. Zhang, M. Aldén, and Z. Li.
Proceedings of the Combustion Institute, 2019, Vol. 37, p. 1337–1344

IV **Infrared Degenerate Four-wave Mixing with Upconversion Detection for Quantitative Gas Sensing**
R. Pedersen, and Z. Li.
Journal of Visualized Experiments, 2019, p. 1–7

V **Characterization of the NEP of Mid-Infrared Upconversion Detectors**
R. Pedersen, L. Høgstedt, A. Barh, L. Meng, and P. Tidemand-Lichtenberg.
IEEE PHOTONICS TECHNOLOGY LETTERS, 2019, Vol. 31, p. 681–684

All papers are reproduced with permission of their respective publishers.

Acknowledgements

The work described in this thesis was performed mostly at the Division of Combustion Physics at Lund University, with a few months spent at the Risø campus of the Technical University of Denmark and at NLIR[1]. During my PhD I have worked with a number of people who I would like to thank for their help, support, and for being a pleasure to work.

I would thank my supervisor Zhongshan Li for his continual support and guidance, and especially for dealing with the final editing and submission of Paper III, so I could go home and pass out on a couch. I would like Peter Tidemand-Lichtenberg, my co-supervisor, for support and guidance, and for always pushing me to better understand nonlinear optics.

It was an absolute pleasure to work with the people at NLIR, and I would like to thank them for making my time there enjoyable. Thanks to Anna-Lena Sahlberg for helping me get started in the lab when I began my work in Lund. During my thesis I shared the lab with Dina Hot, and I appreciate that she has always been professional, effective, organized, and a joy to work with. Thanks Hanyu Ye for his hard work on the OPG project. I would like to thank Merete Styczen and Mathias Christiansen for their help proofreading this thesis.

---

[1] The company producing the upconversion detector described in this thesis.

Populærvidenskabelig Sammenfatning

Forbrænding er en process, der har en central betydning i det moderne samfund. Forbrænding bliver brugt som energikilde i kraftværker og i køretøjer. Men på trods af den vide udbredelse af brugen, er selve forbrændingsprocessen ikke forstået i detaljer. Den overordnede process er selvfølgelig kendt, kulstof og hydrogen reagerer med ilt og bliver til vand og kuldioxid, men mellem de to endestationer foregår der kompleks kemi når molekyler bliver nedbrydt og reagerer med hinanden på kryds og tværs, før forbrændingen ophører. Detaljerne her er ikke fuldt kendt, men de er nødvendige hvis det skal være muligt at regne på hvordan forbrændingen vil foregå når man designer nye motorer eller kraftværker, og dette ville kunne bruges til at optimisere effektiviteten og reducere forurening. Dette er specielt vigtigt for biobrændsler, fordi de ikke har fordelen af årtiers erfaring med motor- og kraftværksdesign.

En af de store barrierer for at forstå flammekemi er udfordringen i at måle, hvad der foregår i en flamme. En hver form for probe, der bliver sat ind i en flamme vil ændre, hvad der foregår i den, og vil derfor ikke nødvendigvis give brugbare målinger. Derfor bliver der i høj grad brugt lys og laser baserede målemetoder inden for flammeforskning, da de kan bruges til at måle uden at flammen forstyres. Disse metoder udnytter at forskellige atomer og molekyler interagerer med lys ved forskellige bølgelængder (farver). Hvilke bølgelængder, der bliver absorberet i eller udsendt fra en flamme, kan derfor sige noget om hvilke stoffer der er i flammen.

Udover absorbtion og emission af lys findes der andre målemetoder, der udnytter ikke-linære fysiske processer. Disse processer finder kun sted ved meget høj intensitet af lys ved en bestemt bølgelænde. Dette kan bruges til få information fra et bestemt punkt i en flamme, da man kun genererer et signal fra det punkt hvor lyset er fokuseret. Det er især til disse metoder at vi har brug for lasere, da de kan levere høj intensitet ved (næsten) en enkelt bølgelængde af gangen. Yderligere kan de være pulsede, med pulser der varer i ekstrem kort tid, for eksempel på nanosekund skala. Det har den fordel at signalet kun bliver genererer mens lyset er der, så man kan få et 'snap-shot' fra en process der ændrer sig hurtigt, lidt som at tage et målfoto i et væddeløb.

Målet med denne afhandling har været at udvikle og implementere ikke-linære målemetoder for infrarødt lys. Grunden til at infrarødt lys er interessant er, at der er visse vigtige molekyler, der ikke kan detekteres med synligt eller ultraviolet lys, men kan måles i det infrarøde. Et eksempel på disse molekyler er methan, der er indeholdt i naturgas og biogas. Et andet eksempel er hydrogencyanid, der bliver genereret når man brænder noget der inderholder nitrogen, hvilket er det meste biobrændsel. Hydrogencyanid er ikke i sig selv et problem, da det bliver forbrændt, men det kan producere NO_x gasser når det bliver brændt, hvilket er kendt for at forårsage kræft ved indånding.

Der er adskillige mindre sideprojekter beskrevet i denne afhandling, men hovedresultatet er at vi nu har demonstreret punktmålinger af hydrogencyanid i en flamme, hvilket kun har været muligt fordi vi har kombineret ikke-linære målemetoder udviklet ved forbrændingsafdeling ved Lund Universitet, og fotonikafdelingen ved Danmarks Tekniske Universitet.

Definitions and Abbreviations

0.1 Definitions

a: [ ] Empirical scaling constant for quantitative DFWM measurements, see Eq. 4.27.
A_{IR}: [V] Amplitude of E_{IR}
A_P: [V] Amplitude of E_P
A_{up}: [V] Amplitude of E_{up}
B: [Hz] Bandwidth.
b: [counts] Mean background level (DFWM).
c: [ms^{-1}]Speed of light in a vacuum.
c_q: [ ] Collisional parameter for empirical PS equation.
$c_{q,1}$ and $c_{q,2}$: [ ] Collisional parameter for empirical PS equation for cases 1 and 2.
d_{eff}: [mV^{-1}] Effective nonlinear coefficient of a nonlinear crystal.
E_i: [J] Energy of energy level i.
E_{IR}: [V] Electric field of the light at wavelength ω_{IR}
E_P: [V] Electric field of the light at wavelength ω_P
E_{ph}: [J] Energy of single photon.
E_{up}: [V] Electric field of the light at wavelength ω_{up}
f: [Hz] Laser frequency.
f_0: [Hz] Center frequency of transition used for PS.
f_1 and f_2: [ ] Mole fraction for case 1 or 2, see Eq. 4.19.
f_N: [ ] Molefraction of the relevant molecular species.
g_i: [ ] Degeneracy of energy level i.
g: [m] Lineshape function.
$g_D(\nu)$: [m] Gaussian lineshape function from Doppler broadening.
$g_L(\nu)$: [m] Lorentzian lineshape function.
g_o: [ ] Spectral overlap parameter for PS.
$g_{o,i}$: [ ] Spectral overlap parameter for PS, for case 1 or 2, see Eq. 4.19.

$g_V(\nu)$: [m] The Voigt lineshape function.
h: [Js] Planck constant.
$\hbar$: [Js] Planck constant ($\hbar = h/2\pi$).
I_1 and I_2: [Wm^{-2}] PS probe beam strength for cases 1 and 2.
$I_{measured}$: [Wm^2] Measured signal strength.
I_P: [Wm^2] Intensity of pump light.
I_{PS}: [Wm^2] Intensity of of the PS signal.
I_{p1}: [Wm^2] Intensity of the high frequency pump used for DFG.
I_{probe}: [Wm^2] Intensity of the probe beam for PS or DFWM.
I_{sat}: [Wm^2] Saturation intensity for DFWM.
I_{sig}: [Wm^2] DFWM signal predicted by the Abrams and Lind equation.
I_{pump}:[Wm^2] DFWM pump intensity (for each pump individually).
$k(\nu, T, p)$: [m^2/molecule] The monochromatic absorption coefficient.
k_B: [J/K] Boltzmann constant. 5
$\mathbf{k}_d$: [m^{-1}] Wavevector of the light generated by DFG.
$\mathbf{k}_{IR}$: [m^{-1}] Wavevector of the infrared signal Eq: 4.2.
$\mathbf{k}_P$: [m^{-1}] Wavevector of the pump Eq: 4.2.
$\mathbf{k}_{p1}$: [m^{-1}] Wavevector of the high frequency pump of DFG.
$\mathbf{k}_{p2}$: [m^{-1}] Wavevector of the low frequency pump of DFG.
$\mathbf{k}_{up}$: [m^{-1}] Wavevector of the upconverted light Eq: 4.2.
L: [m] Interaction length (Length of nonlinear crystals, overlap lengths of laser beams, etc.).
L_l: [Wm] Laser lineshape.
m: [kg] Molecular mass of a molecular species.
N: [m^{-3}] Molecular number density.
n: [ ] Temperature dependence coefficient.
N_0: [ ] Initial number density of the population in the lower rotational level in PS.
n_d: [ ] Refractive index for the light produced by DFG.
n_{IR}: [ ] Refractive index for the infrared signal Eq: 4.8.
n_P: [ ] Refractive index for the pump Eq: 4.8.
n_{IR}: [ ] Refractive index for the high frequency pump of DFG.
n_{IR}: [ ] Refractive index for the low frequency pump of DFG.
n_{up}: [ ] Refractive index for the upconverted light Eq: 4.8.
P_{opt}: [W] Optical power incident on photodetector.
p: [Pa] Pressure.
p_r: [V/W] or [counts/W] Power response of a detector.
p_s: [Pa] Partial pressure.
$Q(T)$: [ ] Partition function at a given temperature.
$\mathbf{r}$: [m] Position vector
S: [$\mathrm{Js}^{-1}\mathrm{m}^{-2}$] Saturation parameter for PS.

$S_i(T)$ [m/molecule] Linestrength of line i at a given temperature.
T: [K] Temperature.
T_{ref}: [K] Reference temperature for HITRAN data.
$\bar{x}_b$: [V] or [counts] Mean background signal of photodiode.
$\bar{x}_s$: [V] or [counts] Mean signal from photodiode.
α: [ ] Experimentally determined scaling constant for an empirical description of the PS signal.
α_0: [m^{-1}] Line center absorption coefficient.
γ_{air}: [m^{-1}Pa^{-1}] Collisional broadening coefficient of air.
γ_L: [m^{-1}] The collisional induced HWHM.
γ_{self}: [m^{-1}Pa^{-1}] The collisional broadening coefficient for collisions of a molecular species with itself.
δ: [rad/s] Normalised detuning from transition line.
ϵ_0: [Fm^{-1}] Vacuum permittivity.
η: [counts/photons] Detection efficiency of detector.
η_s: [W/W] Efficiency of SFG.
η_d: [W/W] Efficiency of DFG.
$\zeta_{JJ'}$: [ ] Transition dependent polarisation factor for PS signal calculation.
θ_{up}: [rad] Angle between the propagation directions of the upconverted light and the pump during upconversion.
θ_{IR}: [rad] Angle between the propagation directions of the infrared light and the pump during upconversion.
Δk: [m^{-1}] Phase-mismatch.
Δk_z: [m^{-1}] z-component of the phase-mismatch.
ΔN_0: [m^{-3}] Population difference between the upper and lower levels in absence of an applied field (DFWM).
Λ: [m] Length of poling period in poled nonlinear crystal.
λ: [m] Wavelength.
λ_d: [m] Wavelength of the light produced by DFG.
λ_{up}: [m] Wavelength of the light resulting from upconversion.
λ_{IR}: [m] Wavelength of the infrared signal.
λ_P: [m] Wavelength of the upconversion pump.
μ: [Cm] Transition dipole moment.
ν: [m^{-1}] Wavenumber.
ν_0: [m^{-1}] Center wavenumber of a given transition line.
ξ: [ ] Extinction coefficient of polarisers used for PS.
$\sigma(\nu, T, p)$: [m^2/molecule] The absorption cross-section.
σ_b: [V] or [counts] Standard deviation of the background output of a photodiode.
ω_d: [rad/s] Angular frequency of light produced by DFG.
ω_{IR}: [rad/s] Angular frequency of the infrared signal Eq: 4.1.

ω_P: [rad/s] Angular frequency of the pump Eq: 4.1.
ω_{p1}: [rad/s] Angular frequency of the highest frequency pump used for DFG.
ω_{p2}: [rad/s] Angular frequency of the lowest frequency pump used for DFG.
ω_{up}: [rad/s] Angular frequency of the upconverted light Eq: 4.1.
τ_1: [s] Population relaxation time (DFWM).
τ_2: [s] Coherence relaxation time (DFWM).

0.2 Abbreviations

AGS: Aluminium Gallium Sulfide (crystal)
BD: Beam dump
BS: Beam splitter
CARS: Coherent anti-Stokes Raman spectroscopy
DFG: Difference frequency generation
DFWM: Degenerate four wave mixing
DM: Dichroic mirror
DME: Dimethyl ether
HITRAN: High Resolution Transmission (database)
HWHM: Half-width Half-maximum
IRPS: Infrared polarisation spectroscopy
IR: Infrared
LD: Laser diode
LIF: Laser induced fluorescence
LITGS: Laser induced thermal grating spectroscopy.
NEP: Noise equivalent power
LP: Long-pass (filter, followed by cut-off wavelength)
OCT: Optical coherence tomography.
PPLN: Periodically poled lithium niobate
PS: Polarisation Spectroscopy
QCL: Quantum cascade laser
RBC: Dark counts per second for photon counter.
SFG: Sum frequency generation
SHG: Second harmonic generation
SP: Short-pass (filter, followed by cut-off wavelength)
SPDC: Spontaneous parametric down conversion
TLAF: Two-line atomic fluorescence
UV: Ultraviolet
WALTHER: Water line thermometry.

Chapter 1

Introduction

Combustion has, for more than a century, been the dominating source of energy for transportation and power production. While efforts are made to replace fossil fuels with renewable energy sources, combustion will for the foreseeable future play a key role. Part of the change to renewable energy sources might be to biofuels, which also requires combustion to release the energy stored in them. It is, therefore, vital to gain an improved understanding of combustion chemistry, to optimize the efficiency and minimize the pollution associated with combustion.

Laser diagnostic techniques are an important tool in combustion research, as they allow measurements throughout a flame with minimal disturbance. In contrast, invasive techniques such as thermocouples, or sampling for mass spectroscopy will change flame structure and composition, which might skew the results. Measuring directly in the flame also ensures that the gas composition does not change due to reactions before measurement. Work with laser diagnostic techniques is generally split into either working on implementing techniques to research a particular flame or engine dynamic, or working on improving the limits of a particular technique. The focus of this thesis is on the latter, in particular by use of upconversion detection together with nonlinear infrared techniques in the mid-infrared region.

The reason for focusing on the infrared is, that a number of species which play an essential role in combustion chemistry do not have absorption features in the visible or ultraviolet, which makes it necessary to go to the infrared to detect them. These species include water, CO_2, sulfate compounds: SO_2, CS_2, H_2S, OCS; hydrogen halides: HCl, HF; small hydrocarbons: CH_4, C_2H_2, C_2H_4, C_2H_5;

and nitrogen compounds: HCN and NH_3. The most successful work presented here have been with detecting HCN, published in Paper III, and the logical next step would be to apply the same technique to NH_3, to quantify the detection limit for this species. Attempts were also made to obtain sources through the Mid-Tech network for the detection of other species, in particular HCl, but we could not obtain sources with a narrow enough linewidth to allow detection of the concentrations we were interested in.

There are some challenges associated with working in the infrared. There are, generally speaking, fewer well developed mid- or far-infrared sources commercially available, compared to what is available in the visible range. This is caused by a combination of a higher degree of commercial interest in laser at shorter wavelengths, and challenges in finding good gain media in the mid- to far-IR, or efficient conversion from near-IR source to longer wavelengths. For the work presented here this has mainly manifested itself in two ways: the low pulse energy stability of the high pulse energy dye laser system we use has limited the precision of measurements, and it has proven difficult or, so far impossible, to obtain laser with the tunability and linewidth required for certain measurements, even within the Mid-Tech cooperation. The second challenge associated with working in the mid-IR, is that the detectors available in this range are noisy and expensive when compared with visible or near-IR detectors. In addition, they suffer from a limited bandwidth and often require cryogenic cooling. The work presented in this thesis address these issues by implementing upconversion detection with the nonlinear infrared signal generation techniques. This uses sum frequency generation to transfer the signal from the mid-IR to the near IR where silicon based detectors can be used. As an added bonus, the high wavelength and angle selectivity of the phasematch condition leads to a large suppression of the background blackbody radiation. The main challenge with this technique is the added complexity, which means that several components must be kept optimised to ensure that the detection efficiency remains constant, which requires regular maintenance. A constant, or at least a known, detection efficiency is of course required for comparing separate measurements.

Part of the focus of this thesis has been on achieving quantitative concentration measurements in flames. For this, stable operation of the signal generating laser and the detection setup is required, in conjunction with a good calibration measurement to translate signal intensity to concentrations. In addition, accurate temperature measurements are necessary, as the expected signal strength from a given concentration has an exponential dependency on temperature. Coherent anti-Stokes Raman spectroscopy is the gold standard for temperature measurements in flame conditions, but there are two drawbacks to using this method.

Firstly, performing CARS requires large and expensive lasers and detectors, as well as a complicated alignment. Secondly, the uncertainty of CARS temperature measurements increases in the range 1000-2000 K, which is the temperature range for most flames. Therefore attempts have been made to develop an alternative approach using waterline structures in the range 3230-3232 cm^{-1}, where there are two transition line groups whose relative intensity changes drastically over the range 1000-2000 K. These lines can be accessed using infrared polarization spectroscopy (IRPS) or degenerate four wave mixing (DFWM), which would make it possible to use the same setup for the concentration measurements and their associated temperature measurement. This in turn, would make it simpler to ensure that the flame conditions are the same, and drastically reduces the time and resources needed for quantitative measurements. This technique is described in more detail in Chapter 4.

This thesis is intended as an introduction to the subject, theory and techniques discussed in Papers I-V. A general introduction to the flames and burners are given in Chapter 2, to make the reader aware what demands and limitations are imposed on the detection methods. The physical feature that form the basis for all infrared spectroscopy is rotational-vibrational optical transitions, and these are discussed in Chapter 3, with focus on how to calculate absorption cross-sections as a function of temperature and pressure. Chapter 4 summarises the basic theory of the nonlinear methods used for this thesis. This expands on Chapter 3 by describing how to use the linestrength and absorption cross-section to calculate the expected signal from IRPS and DFWM, with special focus on applying this for quantitative measurements. Accurate temperature measurements are crucial for accurate quantitative measurements, which is why a section on thermometry is included at the end of Chapter 4. The following chapters function, in part, as an appendix, providing additional details on the upconversion detector (Chapter 5), the lasers used (Chapter 7), and on various minor projects (Chapter 6 and Chapter 7). These might be of interest to the reader, but are not essential to understanding the core of the thesis, which is presented in chapters 2-4.

Chapter 2

Flame and Burner

Despite the current trend towards non-combustion based sources of energy, combustion will remain a significant energy source for the foreseeable future especially when considering the shift towards using biofuels, either purpose made or waste products from other industries. It is therefore still critical to optimize the efficiency of combustion and to reduce the pollution associated with it. While biofuels from a CO_2 perspective is an improvement, they contain much more Nitrogen, Sulphur and various trace salts than fossil fouls, which during combustion can result in the production of NO_x gasses, SO_2, OCS, HCl and other substances that are either harmful when inhaled or corrosive. This shortens the lifespan of the engine or power plant used to extract energy from the combustion process, or the lifespan of the people who are supposed to benefit from it.

The simplest flame to model and measure on, is a laminar flame with premixed gas, as seen on a Bunsen burner. The laminar flow means that, as opposed to a turbulent flame, the flame can be prepared with a well defined steady flame front. This greatly simplifies measurements, as this makes the conditions time independent. Thus it is possible to perform several measurements of concentration and temperature in a single point to reduce the uncertainty, and to perform measurements at different points in the flame sequentially. As opposed to this, measurements made in a turbulent flame in the same point in space but 0.1 second apart might not be correlated at all. Having the gas premixed also greatly simplifies the modelling of the flame, as this removes the need to model diffusion between the two flows with oxygen and fuel.

A typical structure of a premixed laminar flame is shown in Figure 2.1. The premixed gas flows from below and is heated in the preheating zone to the point

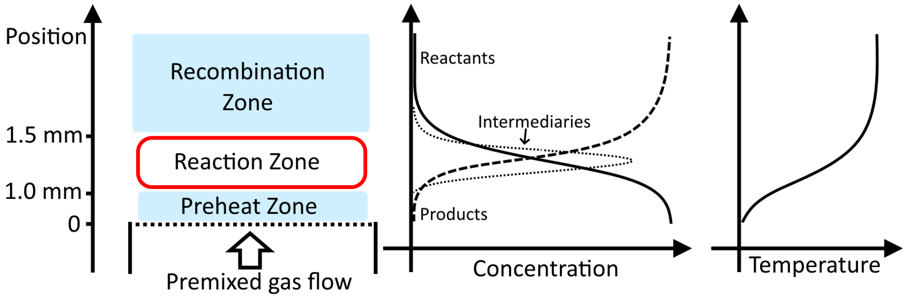

Figure 2.1: To the left is shown the structure of a premixed flame with one dimensional laminar flow. In the middle is shown the concentrations of reactants, intermediary and product species and to the left is shown the change in temperature. Note that the curves are purely sketches for illustration and are not to scale. The values for the positions of the various zones are order of magnitude estimates for atmospheric pressure, for the methane/air flames that have mostly been used during this work.

where the fuel begins to decompose. It then enters the reaction zone, where energy is released as the fuel reacts with the oxygen. The gas temperature increases rapidly across the reaction zone. In the product zone the temperature is still high, but the gas components have reached equilibrium concentrations.

A defining parameter for premixed flames is equivalence ratio, which is the normalized ratio of fuel to oxidizer. An equivalence ratio of $\Phi = 1$ means that the mixture is stoichiometric. The mixture is fuel lean if $\Phi < 1$, which means there is an excess of oxidizer present, and it is fuel rich if $\Phi > 1$, which means there is an excess of fuel present.

We use nonlinear signal generation techniques to study flames, as they provide the spatial resolution necessary to resolve the concentration and temperature changes illustrated in Figure 2.1. However, high laser intensities are needed to drive these nonlinear effects, which limits us to pulsed lasers with low repetition rates. The dye laser system used for the degenerate four wave mixing and polarization spectroscopy described here is based on a flash lamp pumped Nd:YAG laser with a repetition rate of 10 Hz. This means that we can get one measurement each 0.1 s, and that each scan over a few molecular transition lines[1] takes approximately one minute. This timescale limits us to mainly study flames where the structure is time-independent.

For the reasons described above, a McKenna type porous plug burner was used for generating the flame employed for Paper I. This burner delivers a flat 1D flame, where, ideally, the flame only changes as a functions of height, not with radial position. The measurements described in this paper were, in part, performed at low pressure. The advantage of this is that it broadens the flame

---

[1] Usually 1-2 cm^{-1}.

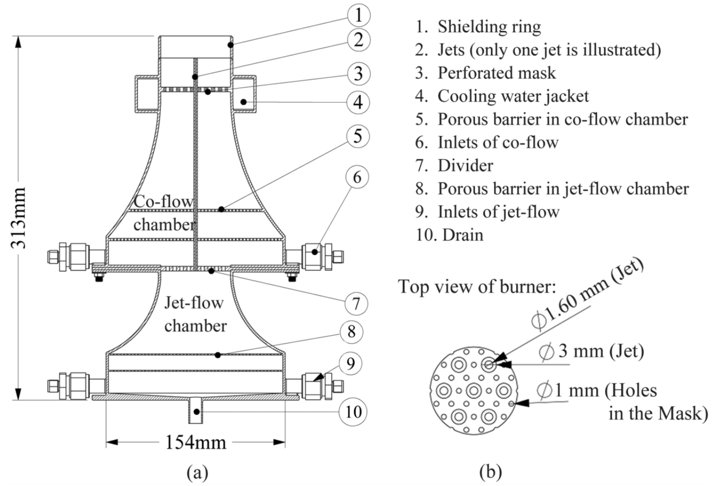

Figure 2.2: Reprinted from [1], with the permission of AIP Publishing. (a) Diagram of the burner. (b) Partial top-down view of the jets and perforated mask.

front from the scale of approximately 100 μm to approximately 1 mm. This allows more measurement points through the flame front, without improving the spatial resolution of the optical setup[2].

Burning solid fuels greatly increases the complexity of the flow dynamics, because the fuel must now first undergo a phase change, from solid to gas state, and then mix with the oxygen. This presented a number of issues that had to be addressed for the measurements of HCN release from pressed straw pellets described in Paper III. To create a stable, laminar flow around the straw pellets we chose to use a multijet burner developed by Weng *et al.*[1], shown in Figure 2.2, which provides a laminar flow in a large area with a stable and adjustable temperature. Even then, the introduction of the ceramic rods used to hold the pellet and the pellet itself induced some turbulence, but the gas flow was still steady enough to perform reproducible measurement. The second issue was that for the solid fuel, as opposed to a premixed gas, we could not continuously feed new fuel in as it was consumed. This meant that the gas concentration was time dependent, changing from the point where a new pellet was introduced till the pellet was consumed, a process of approximately 80 seconds. For this reason it was not possible to scan the laser across the HCN line during the measurement, as the HCN concentration would change significantly during the duration of the scan. Instead the measurement was performed by setting the wavelength

---

[2] The spatial resolution of the IRPS setup used in Paper I was estimated to be $0.5 \times 0.5 \times 10$ mm, and $0.4 \times 0.4 \times 6$ mm for the DFWM setup used in Paper III.

of the laser to the peak of the transition line and measuring the signal at this wavelength as a function of time.

The multijet burner, shown in Figure 2.2 is designed to provide a laminar flow with a homogeneous temperature profile in a 40x70 mm cross section, while allowing seeding of gas or liquid additives. This is achieved by using 181 jets of a premixed fuel/oxygen/buffer gas mixture, with each jet surrounded by a N_2 co-flow. The shape of the chambers and the addition of the porous barriers ensure an equal flow through the jet-tubes and through the perforated mask. The outlet of the burner is 60 mm x 100 mm, but heat loss at the edges limits the homogeneous area to 40 mm x 70 mm.

Chapter 3

Molecular Spectroscopy

The rotation, vibration and electronic states of a molecule are all quantized, with a specific energy associated with each state. A molecule will be in some combination of rotational-, vibrational-, and electronic state, and can transition to another combination when energy is gained or lost through collisions or radiative transfer. The precise energy of a given transition will depend on the specific energy levels involved, but the order of magnitude of transitions between different electronic levels, vibrational levels, and rotational levels are markedly different from each other, as shown in Figure 3.1.

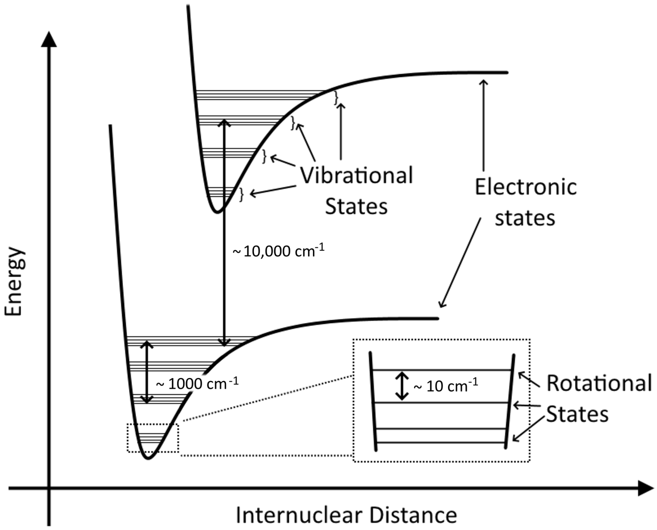

Figure 3.1: Illustration of the electronic, vibrational and rotational energy levels of a molecule.

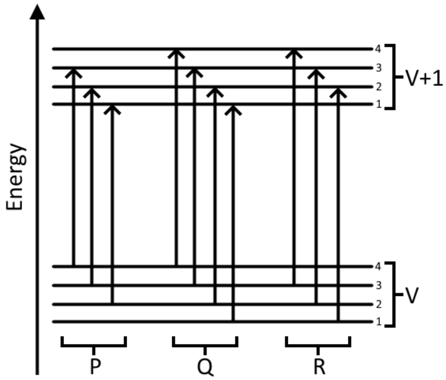

Figure 3.2: Energy diagram showing the difference between the P-, Q-, and R-branches of a vibrational transition. The energy difference between rotational levels have been exaggerated to make it visible on the same scale as the vibrational transition.

The transitional lines in the mid-IR are molecular rotational-vibrational lines, where the transition is only between rotational and vibrational energy levels, with no change in the electronic state. The allowed ro-vibrational states are unique to each molecule, and can therefore be used to distinguish which molecules are present. There are slight differences in the positions of transitional lines of different isotopes of the same molecule, but as each molecule naturally occurs almost completely as one specific isotope[1], only the most common isotope of the molecules discussed here have been included in calculations.

For a transition between two vibrational levels, the majority of the energy difference will be given by the vibrational levels, but the vibrational transition will be split into a rotational fine structure given by the rotational energy levels involved. This structure is split into different branches, which are defined by the change in rotational level. The strongest branches are names the P-, Q- and R-branches, for which the rotational level decreases by 1, is unchanged or increases by 1 respectively[2], as shown in Figure 3.2.

---

[1] The dominating isotope usually makes up 98-99% of the molecules of a specific material, though there are exceptions most notably molecules containing Cl and Br.

[2] For branches with a larger change in rotational level the naming scheme is extended by going to O- and S-branches, and so on.

3.1 HITRAN: Calculating Linestrength and Shape

When using transitional lines for spectroscopy, especially for quantitative measurements, it is necessary to consider the strength of the absorption/emission lines. The strength of a transition depends on the population of the upper and lower level, on the degeneracy of each level and on the overlap of the wavefuntions of the two states. This is not simple to calculate from first principals, but this is not necessary for our purposes, as it has already been done, and the results are available in the high-resolution transmission molecular absorption (HITRAN) database[2, 3, 4, 5]. The HITRAN-database has been constructed over decades of work, and currently covers 49 molecular species, among which are the most common molecules considered in atmospheric and combustion physics. The main focus of the database is, however, atmospheric physics, which means that some of the transition lines that are significant at flame temperatures have been left out, as their linestrengths are negligible at room temperature. The high-temperature molecular spectroscopic database (HITEMP)[6, 7] was initiated to address this issue, and it currently covers H_2O, CO_2, N_2O, CO, NO, NO_2, and OH. It uses the same format as HITRAN, but includes a large additional number of lines that only have significant linestrengths at flame temperatures. H_2O for instance has 281,603 lines listed in HITRAN, but 114,241,164 lines in HITEMP.

The behaviour of a molecule is summarized in its partition function $Q(T)$, which is a sum over all the energy states weighted by their degeneracy and the Boltzmann factor[2]:

$$Q(T) \equiv \sum_i g_i \exp\left(-\frac{E_i}{k_B T}\right) \tag{3.1}$$

where E_i is the energy of energy level i, k_B is the Boltzmann constant, T is the temperature, and g_i is the degeneracy of energy level i. Calculating this is more complicated than immediately obvious from Equation 3.1, but for the purposes of this thesis it is a function of temperature with known values. The linestrengths of transitions for the molecules considered here are available from HITRAN at the reference temperature, $T_{ref} = 296$ K. The linestrength is a function of temperature, as the populations of the upper and lower energy levels change with temperature. $Q(T)$ can be used to scale the linestrength at the reference

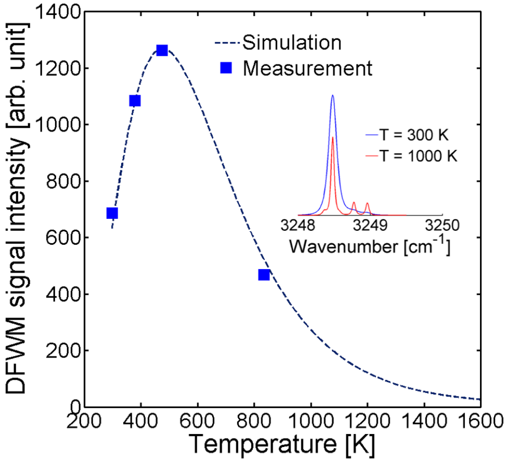

Figure 3.3: Scaling of the degenerate four wave mixing signal with temperature. When the four wave mixing signal is generated from a single transition line, as here, it is approximately proportional to the square of the linestrength. The transition line used here is the P(20) line of the v_1 band of HCN. This figure is reproduced from Paper III.

temperature to determine the linestrength at a different temperature[3][5]:

$$S_i(T) = S_i(T_{ref})\frac{Q(T_{ref})}{Q(T)}\frac{\exp(-E_i/(k_BT))}{\exp(-E_i/(k_BT_{ref}))}\frac{[1-\exp(-\nu_i/(k_BT)]}{[1-\exp(-\nu_i/(k_BT_{ref})]} \tag{3.2}$$

where E_i is the energy of the lower level, ν_i is the energy difference between the upper and lower level, and $S_i(T)$ is the linestrength. The temperature calibration curve from Paper III is reproduced in Figure 3.3, to illustrate the effect of the linestrength scaling on the expected signal.

In this thesis, spectroscopy is performed using a narrow laser to scan across a transition line, or to measure the signal generated at the peak of the transition line. The strength of the signal generated does not depend solely on the linestrength, but also on the lineshape. The two relevant contributors to the lineshape are collisional broadening and Doppler broadening.

3.1.1 Collisional Broadening

Collisional broadening leads to a Lorentzian line shape[5]:

$$g_L(\nu) = \frac{1}{\pi} = \frac{\gamma_L}{(\nu-\nu_0)^2+\gamma_L^2} \tag{3.3}$$

---

[3] When using linestrength data from HITRAN or HITEMP, the linestrengths of different isotopomers have already been scaled to match their relative atmospheric abundance, and we assume this scaling match the isotopomer distribution of the gasses used for our flames.

where γ_L is the collision induced half-width half-max (HWHM). This value depends on the molecular species present, and can lead to a circular problem where accurately measuring the concentrations of molecular species requires knowing how much the lines have been broadened, which in turn requires knowing the accurate concentrations. The HITRAN-database is aimed at atmospheric physics rather than combustion physics, and the collisional broadening is therefore given for air. This does not necessarily match the composition of species in a flame. However, for flames with a concentration of nitrogen similar to air, it can be a decent approximation, in cases where the actual composition cannot easily be determined. In that case, the collisional broadening is given by[5]:

$$\gamma_L(p,T) = \left(\frac{T_{ref}}{T}\right)^n (\gamma_{air}(p - p_s) + \gamma_{self} p_s) \tag{3.4}$$

where n is the temperature dependence coefficient, p is the pressure, p_s is the partial pressure of the species in question, γ_{self} is the broadening coefficient for collisions with members of the same species and γ_{air} is the broadening coefficient for collisions with air. At atmospheric pressure, near wavelengths of 3 μm, this leads to linewidths on the order of 0.1 cm^{-1}. At low pressure, near 30 - 50 mbar, Doppler broadening begins to dominate and linewidths on the order of 0.01 cm^{-1} are obtained. At atmospheric pressure and flame conditions, the lines also become narrower compared to room temperature and atmospheric pressure, because the gas becomes less dense, which reduces the collision frequency and therefore the collision broadening effect. This is illustrated in Figures 3.4a and 3.4b, where γ_L and γ_D is shown[4] for typical pressures and temperatures.

3.1.2 Doppler Broadening

Doppler broadening is the result of the light absorbed or emitted by the molecules being Doppler shifted relative to the observer due to the velocity of the molecules. This results in a Gaussian line-shape. The Doppler broadening HWHM is given by[5]:

$$\gamma_D = \frac{\nu_0}{c}\sqrt{\frac{2k_B T \ln(2)}{m}} \tag{3.5}$$

---

[4] The specific values depends on the molecule and line chosen. The line here was chosen because it was used in the work with the OPG system described in Chapter 7. The global and local quanta of the upper and lower states of this specific transition are: $V''\{0,0,0,0,1,A1\} \rightarrow V'\{0,0,1,0,1,F2\}$ and $Q''\{2,F2,1,-\} \rightarrow Q''\{2,F1,8,-\}$. The format for the local and global quanta used in the HITRAN database is described in [3].

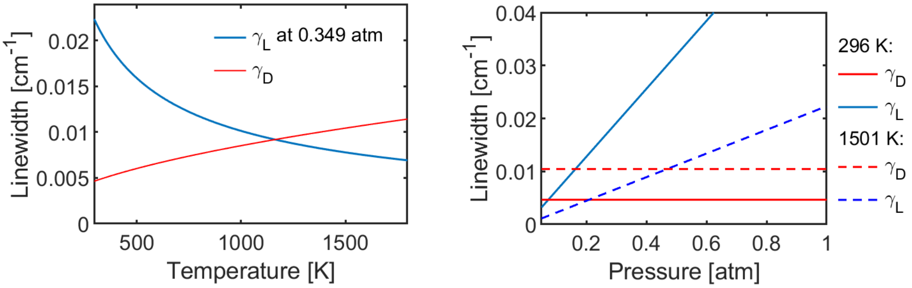

(a) The collisional and Doppler broadened linewidths as a function of temperature for a set pressure, for a methane line at 3018.65 cm^{-1}.

(b) Collisional and Doppler broadened linewidths as a function of pressure for two different temperatures, for a methane line at 3018.65 cm^{-1}.

Figure 3.4

where c is the speed of light, m is the mass of the species and k_B is the Boltzmann constant. The line-shape, is then given by the function[5]:

$$g_D(\nu) = \frac{1}{\gamma_D}\sqrt{\frac{\ln(2)}{\pi}}\exp\left[-\ln(2)\left(\frac{\nu-\nu_0}{\gamma_D}\right)^2\right] \tag{3.6}$$

3.1.3 Voigt

At high pressure, collisional broadening is a much stronger effect than Doppler broadening, while at low pressure Doppler broadening dominates. This means that in most cases the lineshape can be approximated as solely Doppler broadened or solely collisional broadened. In the case where the collisional and the Doppler widths are of the same order of magnitude, the combined effect is found by a convolution of the line shapes of the two, which results in a Voigt lineshape function:

$$g_V(\nu) = \int_{-\infty}^{\infty} g_D(\eta)g_L(\nu-\eta)d\eta \tag{3.7}$$

The monochromatic absorption coefficient $k(\nu, T, p)$ [cm^2/molecule] is then given by:

$$k(\nu, T, p) = S(T)g(\nu, T, p) \tag{3.8}$$

where g is the normalized line shape function and $S(T)$ is the line intensity. The monochromatic absorption coefficient only represents the absorption of a single transition line. Molecules have numerous lines and the complete spectrum is found by taking the sum of the monochromatic absorption coefficients[8]:

$$\sigma(\nu, T, p) = \sum_i S_i(T)g_i(\nu, T, p) \tag{3.9}$$

Where σ is the absorption cross-section. The absorption can then be calculated using the Lambert-Beer law:

$$I = I_0 \exp\left(-N\sigma(\nu, T, p)L\right) \tag{3.10}$$

where N is the molecule number density and L is the interaction length.

3.2 Measuring Laser-Linewidths

The function calculated for $\sigma(\nu, T, p)$ in Equation 3.9 gives the ideal absorption profile. A spectrometer with a very high resolution and a broadband source might be able to approach this, but transition lines for gases are generally narrow, especially at low pressure and the resolution of the measurement instrument must be taken into account. For many spectroscopic measurements, in particular those included in this thesis, a high spectral resolution is achieved by using a tunable laser with a narrow linewidth. This is scanned across the spectral region of interest and the signal intensity is recorded as a function of the laser wavelength. Measuring this way will not yield $\sigma(\nu, T, p)$, but a convolution between the pure absorption spectrum and the laser profile:

$$I_{measured} \propto \int_0^\infty \sigma N L_l d\nu \tag{3.11}$$

where L_l is the laser lineshape. This must be taken into account when evaluating absorption spectra and spectra taken with nonlinear methods. Especially because using a laser that is too broad will flatten the measured absorption structures to the point where they overlap with other absorption features or become undetectable. This makes it important to know the linewidth of the laser used for the measurements. In the absence of a spectrometer with a high enough resolution to accurately measure it, the linewidth can be determined from the signal generated when measuring a well known absorption spectrum. If $\sigma(\nu, T, p)$ is well known, and a good estimate can be made of the laser lineshape[5], $I_{measured}$ can be deconvolved to give a value for the laser linewidth. This has been done to determine the linewidth of the optical parametric generator described in Chapter 7 and as part of some of the Mid-Tech cooperative projects. For this, it is important to keep the pressure in the gas cell at a constant level, as the deconvolution will only give an accurate result if σ is well defined during the measurement.

---

[5] Generally, if it is approximately Gaussian or Lorentzian this can work, if the laser lineshape is broadband and less well ordered deconvolution will be difficult.

Chapter 4

Nonlinear Optics

4.1 2^{nd} Order Effects

Nonlinear optics use a non-linear response of the susceptibility of a material to change the frequency or phase of light. 2^{nd} order nonlinear effects use the second order component of susceptibility. To generate 2^{nd} order effects requires a material without inversion symmetry, which excludes gasses, as the molecules here can move freely, which gives the material inversion symmetry. 2^{nd} order effects are therefore not used for generating the spectroscopic signal directly, but are used for generating the laser pulses used to probe the material, and for converting the generated signal to the range of Si-detectors. The relevant 2^{nd} order processes are difference frequency generation (DFG), sum frequency generation (SFG), and second harmonic generation (SHG), which is the degenerate case of SFG.

4.2 Sum Frequency Generation

SFG is the process of two photons annihilating and creating a new photon at a frequency which is the sum of the frequencies of the two annihilated photons[9, Eq. 21.2-14]. The nomenclature used here is ω_{IR} for angular frequency of the weak infrared signal, ω_P is the angular frequency of the pump, and ω_{up} is the angular frequency of the upconverted light, as this description is in the context of infrared upconversion, where a strong pump is used to upconvert a weak infrared signal. As energy is conserved through the SFG process:

$$\omega_{IR} + \omega_P = \omega_{up} \tag{4.1}$$

The process does not have any inherent need for one photon to be infrared nor any demands for the relative intensity of the two light sources that are combined. For this process to occur to a significant degree the infrared light and the pump must be combined in a crystal with a high nonlinear coefficient, and along a direction which phasematches the three wavelengths[9, Eq. 21.2-15]:

$$\mathbf{k}_{IR} + \mathbf{k}_P = \mathbf{k}_{up} \tag{4.2}$$

where $\mathbf{k}_{IR}$, $\mathbf{k}_P$, and $\mathbf{k}_{up}$ are the wavevectors of each of the three photons. If Equation 4.2 is not satisfied the phase mismatch is given by:

$$\Delta k = \mathbf{k}_{up} - \mathbf{k}_{IR} + \mathbf{k}_P \tag{4.3}$$

The phasematch condition represents conservation of momentum, but it can also be derived by considering the induced polarization. If we consider plane waves of the form:

$$E_{IR} = A_{IR} \exp\left[-i\mathbf{k}_{IR} \cdot \mathbf{r}\right] \tag{4.4}$$
$$E_P = A_P \exp\left[-i\mathbf{k}_P \cdot \mathbf{r}\right] \tag{4.5}$$
$$E_{up} = A_{up} \exp\left[-i\mathbf{k}_{up} \cdot \mathbf{r}\right] \tag{4.6}$$

where E_{IR}, E_P, and E_{up} is the electric field of each wave. A is the amplitude of the electric field indicated by the subscript, and $\mathbf{r}$ is the position vector. The induced polarization of these three waves in a second order nonlinear medium will then contain a component at $\omega_{IR} + \omega_P$:

$$P_{NL}(\omega_{IR} + \omega_P) = 2dE_{IR}E_P = 2dA_{IR}A_P \exp\left[-i(\mathbf{k}_{IR} + \mathbf{k}_P) \cdot \mathbf{r}\right] \tag{4.7}$$

where d is the relevant nonlinear coefficient. This induced polarization will act as a source at the frequency ω_{up}. For the light emitted throughout the nonlinear material to constructively interfere, the phase of the induced polarization must equal the phase of the propagating electric field at ω_{up}, which yields the phase match condition. This generally requires the nonlinear crystal to be birefringent, as the difference between the ordinary refractive index and the extraordinary refractive index can then be used to satisfy Equation 4.2. The problem with this, is that the propagation direction through the crystal is dictated by the phase match condition. This direction will in most cases be different from the propagation direction with the highest nonlinear coefficient.

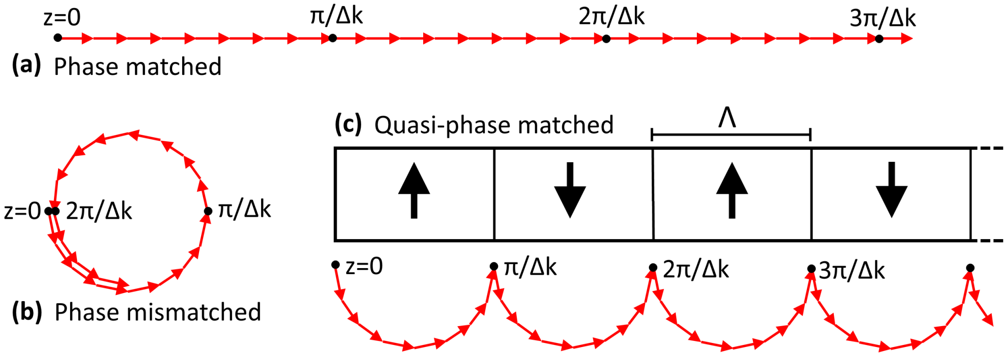

Figure 4.1: Phasors of the light emitted from increments of the nonlinear material. (a): For the phase matched case, all the phasors are aligned, yielding complete constructive interference. The value of Δk here is the value of the mismatch in (b) and (c). (b): In the case of phase mismatch, the phasor direction will change continuously, resulting in complete destructive interference after $2\pi/\Delta k$. (c): Quasi-phase match achieves partial constructive interference by periodically reversing the crystal orientation, and thus the direction of the phasors of the generated.

Quasi-phase matching (QPM) is a way of getting around the limitations set by the phase match condition. At phase match the phasors of the light generated in the nonlinear material will all have the same orientation and add coherently, as shown in Figure 4.1 (a). With a phase mismatch, the phasors of the generated light will change orientation through the material, which accumulates and results in destructive interference, as shown in Figure 4.1 (b). Quasi-phase matching achieves partial coherent interference by changing the orientation of the crystal structure of the nonlinear material periodically, which changes the sign of the nonlinear coefficient. This shifts the phase of the generated light by π, which changes the orientation of the phasors, as shown in Figure 4.1 (c). The period of this shift is called the poling period, Λ. QPM is not as efficient as true phase matching along the same axis would be, but it allows a much wider selection of wavelengths to be phase matched along the direction with the highest nonlinear coeffient. In addition, in most cases the gain from the higher nonlinear coefficient more than makes up for the reduction in efficiency associated with using quasi-phase match instead of true phase-match. For collinear quasi-phase matching, the matching frequencies and poling period are governed by the scalar equation[9, Eq. 21.2-34]:

$$\omega_{IR} n_{IR}(T) + \omega_P n_P(T) + \frac{2\pi c m_H}{\Lambda} = \omega_{up} n_{up}(T) \tag{4.8}$$

where $n_{IR}(T)$, $n_P(T)$, and n_{up} are the refractive indexes for each wavelength at the temperature T. c is the speed of light in a vacuum. m_H is the harmonic order of the quasi-phasematch, and as the efficiency of the process decreases as $1/m_H^2$, only the first order has been used for the work presented here, so $m_H = 1$.

Assuming infinite plane waves, no saturation effects and no pump depletion, the power-to-power efficiency of the quasi phase-matched SFG process is given by [10, P88]:

$$\eta_s = \frac{P_s}{P_{IR}} = \frac{32 d_{eff}^2 L^2 I_P}{\epsilon_0 m_H^2 n_{up} n_P n_{IR} c \lambda_{up}^2} \cdot \operatorname{sinc}\left(\frac{\Delta k L}{2}\right) \tag{4.9}$$

where d_{eff} is the effective nonlinear coefficient[1], L is the length of the periodically poled structure, I_P is the pump intensity, ϵ_0 is the vacuum permittivity, and λ_{up} is the wavelength of the upconverted light. P_s and P_{IR} are the upconverted and infrared power, respectively. Δk is the phase mismatch given by

$$\Delta k = \omega_{up} n_{up}(T) - \omega_{IR} n_{IR}(T) - \omega_P n_P(T) - \frac{2\pi c m_H}{\Lambda}. \tag{4.10}$$

The assumption of no pump depletion is quite accurate for most applications of the upconversion detection applications discussed here, as it is mainly used for weak signals, where even 100% conversion would result in negligible depletion of the pump. The assumption of infinite plane waves on the other hand, does not accurately represent reality. The SFG efficiency is limited by the overlap between the pump beam and the signal beam. The overlap depends on the focusing, and maximizing it requires optimising the focus of the signal beam to match focus position of the pump beam, while simultaneously achieving the ideal beam waist[2]. In addition, the highest conversion efficiency is reached if the transverse profile of both beams are fundamental Gaussian. This is the case for the pump beam, but the beam profile of the signal beams from DFWM and IRPS have not been measured. In practice Equation 4.9 is therefore used to calculate the upper limit that can be expected for the conversion efficiency, and the achieved result will be a factor 2 to 10 lower.

The description so far have assumed that all waves are collinear, but this need not be the case. The theory of non-collinear phasematching is described in detail

---

[1] The value of d_{eff} depends on the material, and the propagation direction and polarization of the light, and can be calculated from the nonlinear coefficients of the material tensors. I will not describe how to calculate this here, as it has been described in both [9] and [10].

[2] The optimal focussing depends on the Rayleigh lengths and wavelengths of both beams, and can be calculated for the fundamental Gaussian mode using the work of Boyd and Kleinman[11] for the signal. However, the transverse mode of the dye laser system used here is not Gaussian. In practice it is better to optimize the conversion efficiency by varying the focal length, starting with a focal length that would make the two beam waist approximately equal, if both had a fundamental Gaussian transverse mode.

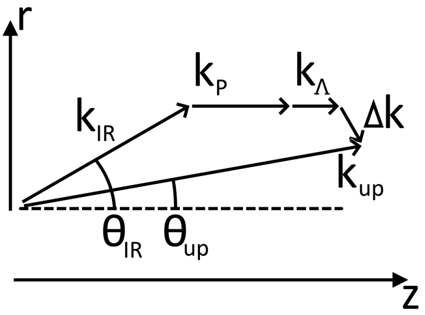

Figure 4.2: k-vector addition for non-collinear phasematching in a periodically poled material.

elsewhere[12]. The situation relevant for this thesis is where the wavevectors of the pump and poling period grating are parallel, with the IR- and upconverted beam at an angle to these. In this case the vector equation for the phasematch can be reduced to a scalar form by projection onto the r- and z-axis shown in Figure 4.2. The phasematch equations then becomes:

$$\frac{\Delta k_z}{2\pi c} = \frac{n_{up}}{\lambda_{up}}\cos(\theta_{up}) - \frac{n_P}{\lambda_P} - \frac{n_{IR}}{\lambda_{IR}}\cos(\theta_{IR}) - \frac{1}{\Lambda} \tag{4.11}$$

$$\frac{\Delta k_r}{2\pi c} = \frac{n_{up}}{\lambda_{up}}\sin(\theta_{up}) - \frac{n_{IR}}{\lambda_{IR}}\sin(\theta_{IR}) \tag{4.12}$$

This is used in Chapter 6 for upconverting two beams at the same wavelength simultaneous, while separating the signals spatially on the detector.

4.3 Difference Frequency Generation

Difference frequency generation can be regarded as the reverse of SFG. For DFG, a high energy pump photon, of frequency ω_{p1}, decays into two lower frequency photons, of frequencies ω_{p2} and ω_d, where $\omega_{p2} > \omega_d$. The main use of this process is to generate laser light at wavelengths, often in the IR, that cannot be reached directly, due to the lack of good laser gain media for those wavelengths. It is this process that is used to reach IR wavelengths in both the pulsed IR dye laser system, which has been used for most of the work presented here, and in the OPG setup[3].

The physics of DFG is very similar to SFG, and the equations describing it are therefore almost identical to the ones describing SFG. The energy conservation

---

[3] Both of these are discussed in more detail in Chapter 7

requirement is essentially the same as given in Equation 4.1:

$$\omega_{p1} - \omega_{p2} = \omega_d \Rightarrow \omega_d + \omega_{p2} = \omega_{p1} \tag{4.13}$$

and similarly for the phasematch condition:

$$\mathbf{k}_d + \mathbf{k}_{p2} = \mathbf{k}_{p1} \tag{4.14}$$

For the case of collinear quasi-phasematching the phasematch condition can be reduced to a scalar equation[9, P. 893-914]:

$$\omega_{p2} n_{p2}(T) + \omega_d n_d(T) + \frac{2\pi c m_H}{\Lambda} = \omega_{p1} n_{p1}(T) \tag{4.15}$$

The efficiency of this process, assuming infinite plane waves, $m_H = 1$, and no pump depletion, is given by[10, P. 88]:

$$\eta_d = \frac{32 d_{eff}^2 L^2 I_{p1}}{\epsilon_0 n_{p1} n_{p2} n_d c \lambda_d^2} \cdot \text{sinc}\left(\frac{\Delta k L}{2}\right) \tag{4.16}$$

4.4 3rd Order Effects

For 3^{rd} order effects, 4 optical waves interact with each other through the third order term of the nonlinear susceptibility. As opposed to 2^{nd} order effects, 3^{rd} order effects can be generated in materials with inversion symmetry, which means that they can be generated in gasses and be used for gas spectroscopy. As for other nonlinear interactions, they have requirements for high intensity and phasematch, which can be used to limit the nonlinear interaction to a certain volume of space. This makes nonlinear techniques especially useful for combustion research, as it makes it possible to achieve three dimensional spatial resolution[4]. This is necessary in the study of laminar flames, as these have a high degree of spatial structure, with large variations in concentration and temperature over short distances. While there are a number of techniques that can be used to achieve spatial resolution in flames[5], this thesis will focus on infrared polarisation spectroscopy (IRPS) and degenerate four wave mixing (DFWM).

---

[4] The spatial resolution of the IRPS setup used in Paper I was estimated to be $0.5 \times 0.5 \times 10$ mm, and $0.4 \times 0.4 \times 6$ mm for the DFWM setup used in Paper III.

[5] Laser induced fluorescence (LIF), coherent anti-Stokes Raman spectroscopy (CARS), and laser induced thermal grating spectroscopy (LIGS), among others.

4.5 IRPS

Initially, polarisation spectroscopy (PS) was developed with particular focus on the application as a sub-Doppler technique[13], with counter-propagating pump and probe. It was first implemented in flames as a method of measuring high temperature spectra of diatomic molecules[14], which otherwise could not easily be prepared in a hot gas flow. The first investigation of its use for flame diagnostics was published in 1986[15].

The sub-Doppler capabilities of the counter-propagating pump probe geometry was, however, quickly abandoned in favour of the co-propagating geometry, which sacrifices the sub-Doppler resolution for higher signal. This was used, in flames, with sources in the visible and UV to detect OH[16, 17, 18], C_2[19], NH_3[18] and CO[18]. For OH, it was even expanded from point detection to 2D imaging[17]. These efforts were useful for determining line positions and for measuring relative signal strengths, for instance for thermometry, but none of them managed to perform quantitative measurements. This was in part due the fact that there is no simple analytical expression for the PS signal, and in part due to the difficulties of performing proper calibration measurements on radicals such as OH and C_2.

Much of the early work was limited to the UV and visible spectral regions, due to a lack of appropriate IR sources. In the last twenty years, PS has expanded into the IR region, as IR laser sources have become available. This makes it possible to detect species which lack electronic transition in the visible and near UV. The reason these species lack these transitions is that, in contrast to radicals, each atom has formed a closed electronic shell by bonding to other atoms. However, the molecules thus formed are chemically stable, which makes it possible to perform calibration measurements in well prepared samples, with known concentrations. This, of course, greatly simplifies quantitative measurements.

The early work in the mid-IR focussed on CO_2[20, 21, 22] at 2 µm and CH_4[23] near 3 µm. This established that mid-infrared PS (IRPS) had a higher sensitivity than laser induced fluorescence (LIF) in the same region, as well as determining the PS lineshape to be Lorentzian cubed. To perform quantitative measurements it was necessary to investigate the effect of varying pump intensity as well as the signal dependency on concentration and buffer gas pressure, which was done for methane and acetylene[24, 25]. This culminated in the first quantitative measurement in flame using IRPS[26] of C_2H_2, and later HCN[27], the latter of which was the foundation for the work presented in Paper III. IRPS was also used for measuring H_2O and OH[28], as well as HF[29], which,

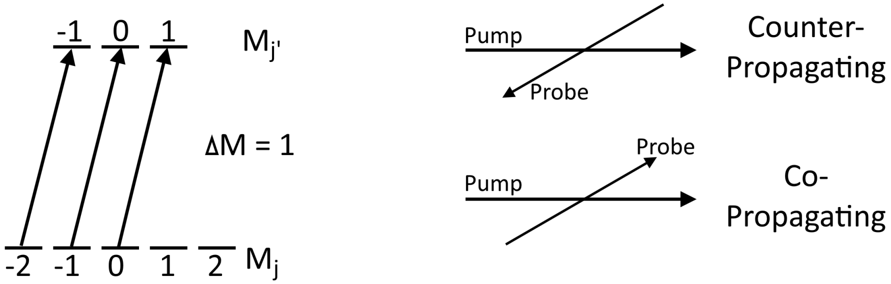

(a) M levels for a P transition with j' = 1 → j = 2.

(b) In the counter propagating scheme the pump and probe travel in opposing direction, which provides sub-Doppler resolution. In the co-propagating scheme they travel in the same direction, which increases the generated signal compared to counter propagation.

Figure 4.3

due to the use of a strong fundamental transition, could be measured in a plane, allowing 2D imaging.

4.5.1 IRPS: Theory

Polarization spectroscopy uses a saturation effect to measure the presence and concentration of a molecule in a certain gas volume. A pump beam of either circular or linear polarisation will, due to selection rules, drive transitions between some values of the magnetic quantum number, M, and not others, as shown in Figure 4.3a. With a strong, saturating pump, this will create a nonuniform population of the magnetic sublevels, which makes the material anisotropic. This in turn makes the material birefringent. By passing a probe beam, with a known polarization, through the volume the degree of birefringence can be probed by measuring the change in polarisation. The strength of the birefringence in gas will depend on the number density of the molecular species in question, which makes it possible to use IRPS for molecular concentration measurements.

The general theory of PS has been treated in detail[30]. Most often a counter-propagating arrangement is used as shown in Figure 4.3b, as the signal generated this way is not Doppler broadened, which is one of the major advantages of PS. Assuming counter-propagating pump and probe beams, and monochromatic laser fields, an analytical expression for the PS signal intensity is given by[31]:

$$I_{PS} = I_{probe}\left[\xi + \frac{L^2 N_0^2 \sigma^2 I_{pump}^2 \zeta_{JJ'}^2}{16S^2(1+4(f-f_0)^2/\gamma_s^2)}\right] \tag{4.17}$$

where S is a saturation parameter[32], L is the length of the interaction region of the pump and probe beams, and N_0 is the population of the initial rotational level. I_{pump} and I_{probe} are the intensity of the pump beam and probe beam, respectively. $\zeta_{JJ'}$ is a factor which depends on the upper and lower J values, and the polarization of the pump beam. Quantitative expressions for $\zeta_{JJ'}$ can be found in [30, 33], but in short using a circularly polarized pump beam enhances the signal strength from P- and R-branch transitions, while suppressing the signal from Q-branch transitions, and vice versa for a linearly polarized pump beam. f_0 is the center frequency of the transition line, f is the center frequency of the laser line, and γ_s is the absorption line width without Doppler broadening. ξ is the extinction coefficient of the crossed polarisers.

However, when using PS for quantitative measurements in the mid-infrared, there are a number of issues which make Equation 4.17 ill-suited. In the mid-infrared, the effect of Doppler broadening is small[6], which means we can afford to use a co-propagating setup, which sacrifices sub-Doppler resolution, but increases the strength of the generated signal. A second issue is that Equation 4.17 assumes a monochromatic laser field, while in practice the linewidth of the laser we use so broad[7] that the overlap between the laser line and the transition line must be taken into account when calculating the signal strength. A third consideration is that it is generally preferable to use pump intensities above the saturation intensity, as this greatly reduces the collisional quenching effects[34, 35]. Assuming saturation intensity, and a stable probe and pump intensity, makes it possible to simplify the expression. With this in mind, an empirical equation for the IRPS signal has been developed [26, 27], which was used for the quantitative measurements described in Paper I :

$$I_{PS} = \alpha \cdot c_q \cdot g_o \cdot I_{probe} \cdot \zeta_{JJ'}^2 \cdot N^2 \cdot \sigma^2 \tag{4.18}$$

This equation describes the line integrated signal. g_o is a spectral overlap parameter, accounting for the overlap between the spectral profiles of the laser and the transition line. The parameter c_q accounts for collisional quenching, and depends on the gas conditions. α is an experimentally determined scaling constant.

Calibration measurements are needed to determine the values of c and g. α and $\zeta_{JJ'}$ cancel out by keeping the factors they represent constant between the

---

[6] The Doppler broadened width scales linearly with the center frequency, see Equation 3.5.

[7] The laser linewidth of IR pulses produced by the dye laser system is estimated to be less than 0.04 cm^{-1} wide.

calibration measurement and the flame measurement[26, 27]:

$$f_2 = f_1 \frac{T_2 \sigma_1 \sqrt{g_{o,1} c_{q,1} I_2}}{T_1 \sigma_2 \sqrt{g_{o,2} c_{q,2} I_1}} \tag{4.19}$$

The subscripts refer to: (1) a calibration measurement with a known concentration and (2) a flame measurement. f_i is the mole fraction of the species measured and T_i is the temperature in the measurement volume.

Equation 4.19 was used in Paper I for quantitative measurements. Because the signal does not depend on the absolute value of c_i, and g_i, but on the ratio between the values at the calibration condition and the values at flame conditions only the ratios need to be determined. The spectral overlap parameter ratio, g_1/g_2, was obtained by measuring the width, in frequency, of the PS signal peak as a function of temperature and pressure. This was then used to the relative value of g under flame conditions. The collisional quenching behaviour was investigated by comparing the signal from CH_4 in different buffer gasses at atmospheric pressure and at 37 mbar. It was found that at 37 mbar the dependence on the buffer gas environment was very weak, and as the average time between collisions only increased with increasing temperature, it was estimated that $c_1/c_2 \approx 1$. The lack of change in c is due to the low pressure for both the calibration and flame measurement. For the same measurement done at atmospheric pressure the change in c between room temperature and flame conditions would be much larger. The intensity of the probe beam is unchanged between the calibration and flame measurement, so $I_2/I_1 = 1$

4.5.2 IRPS: Setup

A diagram of the IRPS setup is shown in Figure 4.4. The collimated mid-IR beam from the pulsed dye laser system, described in Chapter 7, is focused by lens L_1, such that the focal point of the pump and probe beam lie over the burner[8]. A CaF_2 window is used as a beam splitter (BS), the 7% surface reflection is used as the weaker probe beam[9], while the transmitted beam is used as the pump. The pump is passed through a $\lambda/2$ or $\lambda/4$ waveplate, to provide a linearly or circularly polarized pump beam. The pump beam then crosses the probe beam over the burner at a 4° angle, before terminating in a beam dump. The probe

---

[8] As there is a path length difference between the pump and probe the position of the focal point will not coincide completely, but the difference is small enough to be negligible, as the beam is weakly focused and the path length difference is small compared to the focal length.

[9] This window is not wedged, and there is a reflection from the back-facet, but this is removed using an iris, which is not shown in the diagram.

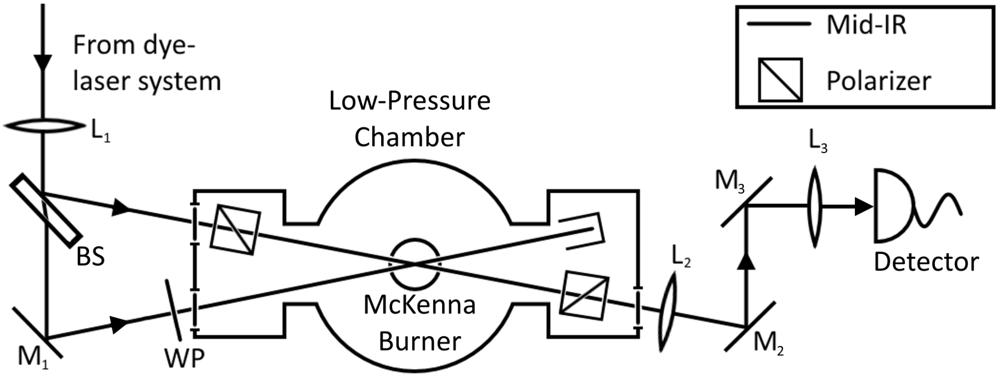

Figure 4.4: Diagram of the polarization spectroscopy setup. BS: Beamsplitter, here a 7% reflective CaF_2 window. M_1-M_3 are gold mirrors. L_{1-3} are uncoated CaF_2 lenses, with focal lengths of 750 mm, 1000 mm, and 100 mm, respectively. WP: waveplate. The detector is time-gated to match the pulses from the laser. The windows in the low-pressure chamber are uncoated CaF_2.

beam is passed through a polariser to ensure the polarization is linear. The probe beam is blocked by the second polariser, which is at a 90 ° angle to the first. The extinction coefficient of the crossed polarisers is on the order of 10^{-7}. If an anisotropy is induced at the crossing point by the pump, the probe beam will change polarization slightly, allowing more light to pass through the second polariser. This is the signal beam, which is collimated by lens L_2, and then directed to the detector

The setup shown in Figure 4.4 is built to allow IRPS at low pressure. Because anisotropy can be induced in materials by stress, it is necessary that there are no windows between the two polarisers. This is achieved here by constructing the low-pressure chamber with space for the polarisers in two side chambers to the main low-pressure chamber. The polarisers and windows are kept clean of soot or condensation by a N_2 flow into each side-chamber, which keeps the gasses in the main chamber from flowing into the side-chambers. The combustion products are extracted by a vacuum pump above the burner.

4.6 DFWM

Degenerate four wave mixing was first described in 1978 by Abrams and Lind[36, 37]. Later, numerous theoretical studies were published investigating the effects of pump intensity[38, 39] polarization[40], spectral broadening effect[41, 42, 43] and how to calculate DFWM spectra with this information[44].

Most of this work were done for the backwards pumped, phase-conjugate configuration, shown in Figure 4.5a. This configuration allows for sub-Doppler resolution, but the forward pumped geometry, shown in Figure 4.5b, provides a relatively higher signal[45].

DFWM was first implemented for flame diagnostics in 1985 for sodium atoms[46], and in 1986 for the OH radical[47]. The first work performed using the forward pumped geometry in flames were done by Bervas in 1992[48].

DFWM performed in the UV region has mainly focused on the detection of OH[49, 50] and NO[49, 51, 52], while detection of NH_3 has also been demonstrated[53]. While the nonlinear characteristics of DFWM generally restricts the use to detection in a single point, due to the need for a high intensity field, 2D imaging of the OH radical has been demonstrated[50].

Due to the success of measuring OH spectra with DFWM, it was considered as an alternative or supplement to CARS[48]. Temperature measurements were demonstrated using 2D-DFWM[54], where the signal from two different rotational transitions were used to image the temperature distribution in a plane. Ideally the signal from both transitions should be acquired simultaneously, however this was not demonstrated here. Multiplex measurements of different rotational transitions in the UV have, however, been demonstrated for point measurements by using a broadband pump[55, 56], which allowed for single shot temperature measurements.

There are a number of species which do not have electronic transition to facilitate detection in the visible or UV region. For these species it is instead necessary to use ro-vibrational transitions in the infrared. DFWM has been used in the IR for detection of various small hydrocarbons: CH_4[57, 58, 59], C_2H_2[57, 60, 58, 61, 59], C_2H_4 [59], C_2H_6 [59], CH_3OH [62], and CH_3Cl [63]; for halides: HF[64] and HCl[61, 65]; nitrogen containing species: NO_2 [65], N_2O [58], and NH_3 [66]; as well as for CO_2 [58]. Paper III has expanded this list by adding HCN.

4.6.1 DFWM: Theory

The theoretical treatment of DFWM signal generation was first developed by Abrams and Lind[36, 37], using a plane wave approximation for the four fields. Their treatment assumes the phase-conjugate pump geometry, while the work presented here use the forward pumped geometry. It will however serve as a basis to discuss the important parameters, as it is more easily interpreted than the full expression for the forward pumped geometry[39]. The equation for the DFWM signal below is taken from [67], which has restated the original Abrams

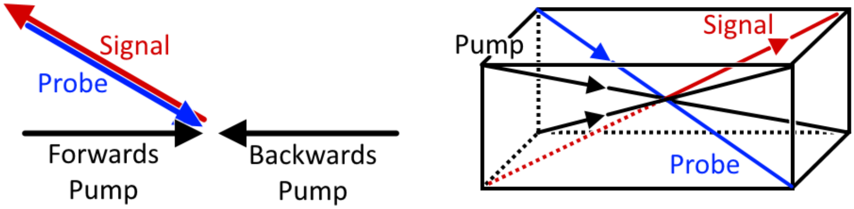

(a) DFWM with phase conjugate pump geometry. **(b)** Forward pump geometry for DFWM.

Figure 4.5

and Lind result slightly:

$$I_{sig} = \frac{\alpha_0^2 L^2}{1+\delta^2} \cdot \frac{4I_{pump}^2/I_{sat}^2}{\left(1+4I_{pump}/I_{sat}\right)^3} I_{probe} \tag{4.20}$$

where L is the interaction length[10], I_{pump} is the pump laser intensity, I_{probe} is the probe laser intensity, I_{sat} is the saturation intensity, δ is the normalized detuning, and α_0 is the line center absorption coefficient. The latter three are given by:

$$I_{sat} = \frac{\hbar^2 c\epsilon_0}{2\tau_1\tau_2\mu^2}(1+\delta^2) \tag{4.21}$$

$$\delta = (\omega - \omega_0)\tau_2 \tag{4.22}$$

$$\alpha_0 = \frac{\mu^2 \Delta N_0 k \tau_2}{2\epsilon_0 \hbar} \tag{4.23}$$

where μ is the transition dipole moment, ω_0 is the line center frequency, k is the magnitude of the wavevector, ϵ_0 is the vacuum permittivity, τ_1 & τ_2 are the population and coherence relaxation times, respectively, and ΔN_0 is the population difference between the upper and lower energy levels, in the absence of an applied field.

The most important result that can be seen from Equation 4.20 is that the signal is very sensitive to the laser intensity when $I_{pump} << I_{sat}$. However, for $I_{pump} \approx I_{sat}$ and $I_{probe} \approx I_{pump}$, the signal is approximately proportional to the pump intensity. Compared to the cubic dependency at low intensity, this makes the signal relatively insensitive to the laser intensity. The reduced sensitivity makes it possible to perform measurements without compensating for small fluctuations

---

[10] Due to the plane wave approximation, the fields overlap everywhere, so the interaction region is limited by the extend of the nonlinear material.

in laser pulse energy. Operating near or above saturation has the additional benefit of reducing the collisional quenching sensitivity significantly[11][68].

While the analytical expression in Equation 4.20 provides a good understanding of the factors contributing to the DFWM signal, it can in practice be difficult to precisely determine all the components of the expression for accurate calculations. For the quantitative measurements in Paper III we therefore take our starting point in a simplified empirical relation [36, 37, 69]:

$$I_{DFWM} \propto \sigma(\nu)^2 N^2 \tag{4.24}$$

where $\sigma(\nu)$ is the absorption cross section for the wavenumber, ν, and N is the total number density of the gas. This assumes the relation $\sigma^2 \propto \mu^4$, which is a good assumption for pump intensities above the saturation level[69], but not for low pump intensities. In addition, it also assumes that the laser pulse energy is stable enough for any fluctuations to be negligible.

When calculating the DFWM signal, it is important to take all nearby transition lines into account, as the DFWM signal generated from each have been shown to add coherently[42] in theoretical studies, as well as experimentally[44, 70]. The monochromatic absorption coefficients for each transition are therefore summed together, before they are squared:

$$I_{DFWM} \propto \left(\sum_i S_i g(\nu) \right)^2 N^2 \tag{4.25}$$

This simplified relation gives the idealized DFWM spectrum, but the signal detected for actual measurements will be the convolution of this spectrum with the lineshape of the pump laser:

$$I_{DFWM} \propto s(T) = \int_{\nu_l}^{\nu_h} \left(\sigma(T,\nu)N(T)\right)^2 L_l(\nu,\nu_0)d\nu \tag{4.26}$$

where L_l is an estimate of the laser lineshape centered at ν_0. The upper and lower boundary of the integral, ν_h and ν_l are chosen to be wide enough to include the contributions of any nearby transitions. The reason why this integral must be evaluated as a function of temperature, is that the lineshape changes with temperature, which in turn means that the overlap with the laser line changes. The transition lineshape generally becomes narrower with increasing temperature, as the gas becomes less dense with temperature at constant

---

[11] The reason for the reduced impact of collisional quenching at high intensity is that the timescale for returning a quenched molecule to the pumped state is so short, that the quenching ceases to have a significant impact on the signal.

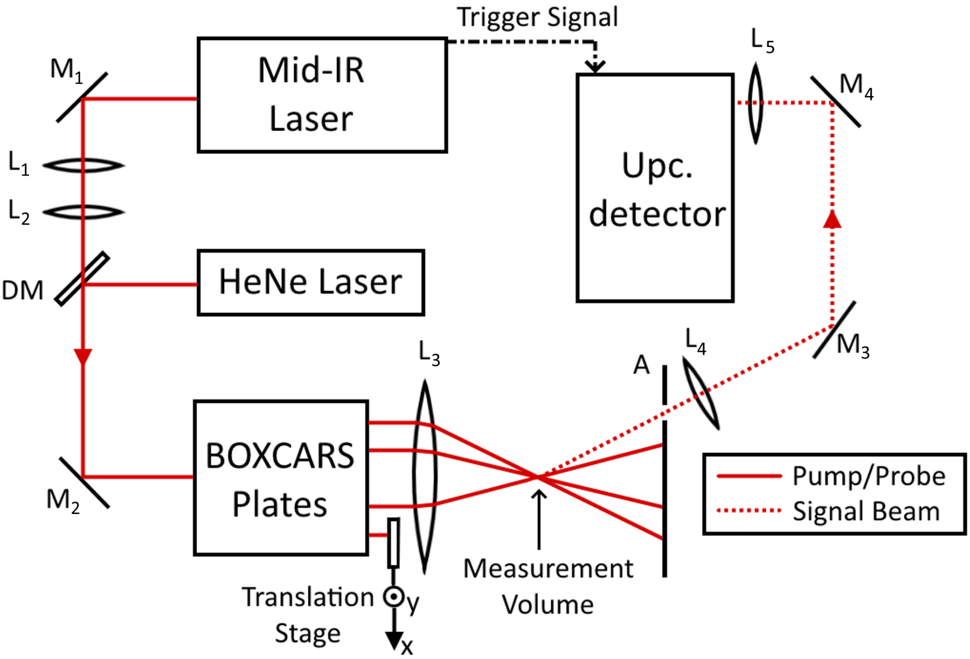

Figure 4.6: Diagram of the DFWM setup. M$_i$ are mirrors, L$_i$ are lenses. **A** indicates the aperture used to block the pump and probe beams. DM: dichroic mirror. The beam block used to block the signal beam is mounted on a translation stage, to allow fine adjustment of the position.

pressure. This reduces the collision frequency, despite the higher speed of the individual molecules. This is a beneficial effect as it increases the overlap and therefore the signal, somewhat countering the reduction in signal expected from the decreasing number density.

To this expression is introduced two terms which take experimental factors into account:

$$I_{DFWM}(T, f_N) = as(T)f_N^2 + b \tag{4.27}$$

where a is a constant particular to a given setup, determined by calibration, which takes into account any material constants, how well aligned the DFWM overlap is, the detection efficiency of detector used, and other variables that depend on the particular setup. f_N is the fraction of the gas which is the species with the transition line used to generate the DFWM signal. b represents the mean value of the background noise from scattered light.

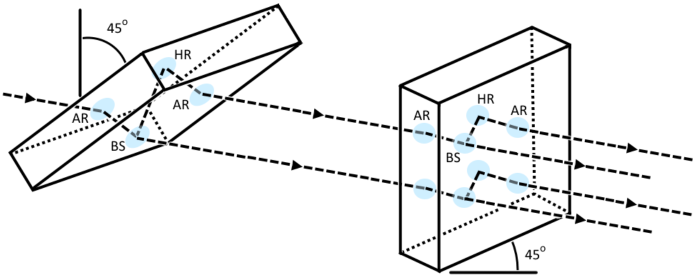

Figure 4.7: The BOXCARS set consists of two identical CaF_2 plates coated for anti-reflection (AR), high reflection (HR), and 50% reflection 50% transmission (BS). When placed in series with one tilted 45° to the vertical and the other 45° to the horizontal, they facilitate splitting one beam into four parallel beams.

4.6.2 DFWM Experimental Setup

A diagram of the experimental setup, as used for DFWM in Paper III, is shown in Figure 4.6. The dye laser system will be described in Chapter 7. The IR pulses are overlapped with a 632 nm continuous wave HeNe beam, to facilitate the alignment. The beam then passes through the pair of BOXCARS plates, as shown in Figure 4.7, to separate the beam into four parallel beams, spaced as the four corners of a square with approximately equal intensity. One of these is selected as the signal beam, they are equal in power, so the choice is arbitrary. The beam passing through the plates with no reflections is chosen, as the guide beam is the most visible for this beam[12]. The four beams are focussed using lens L_3. This both bends the path of the beams, such that they meet in a single point, and focusses each individual beam, such that the beamwaist of each lie in the point where the beams meet. In addition, the beams must converge at equal angles to the central axis. To achieve this, it is important that the beams are equally spaced around the centre of the lens, and that the beams are well collimated and parallel when hitting the lens. The signal beam is then collimated by lens L_4, and directed to L_5 which focusses the signal beam into the upconversion detector. After alignment, the beamblock is placed to block the signal beam, so only the signal generated in the volume where the beams overlap reach the detector. Precise adjustment of the position of the beamblock is necessary, as the other three beams will diffract or scatter from the edges of the beamblock. This is the main source of the background noise limiting the sensitivity of the measurement. For the work done in Paper III, either a heating tube[71, page 23] with a controlled gas flow or a multijet burner[1] was placed

---

[12] The HR and HT coatings are made for the mid-IR wavelength range, not 632 nm, so the guide beam suffer large losses on each pass.

in the measurement area. The multijet burner was used to heat pressed straw pellets to induce gasification and combustion.

4.7 Thermometry

The importance of temperature for quantitative measurements can be seen from Equation 4.26, which shows that the strength of the DFWM depends exponentially on the linestrength. Any DFWM measurement that aims to quantify concentrations must therefore be accompanied by a temperature measurement of the probed volume. There are a number of techniques available for thermometry, each with their own advantages and disadvantages: coherent anti-Stokes Raman spectroscopy (CARS)[72, 73], laser-induced fluorescence (LIF)[74, 75], two-line atomic fluorescence (TLAF)[76, 77], laser-induced thermal grating spectroscopy (LITGS)[78, 79, 80], DFWM probing of OH[54, 56], and DFWM or IRPS probing of mid-IR water lines for thermometry (WALTHER)[81].

CARS is a very well developed technique for temperature measurements. Its advantages include high spatial resolution, the possibility of single shot measurements, high accuracy[13], it can give information about the populations of rovibrational states without using mid-IR lasers, absorption effects are negligible, and the generated signal is directional making it possible to remove much of the background by spatial filtering. The intensity requirements of the technique have made it more applicable to measurements in a single point, but measurements along a line or in a plane have been demonstrated. The downsides to this technique are that it generally relies on the presence of high number density of N_2 for its signal, and it does not perform as well at low pressures. In addition, the setup required is expensive in both components and alignment time, and signal interpretation is not simple.

LIF uses the ratio between rotational subdivision of electronic transitions of species such as OH and NO to measure population distribution and thereby temperature. The advantage of this technique is that it does not require a high intensity to drive weak nonlinear effects, which is why the laser used can be formed into a sheet, allowing temperature measurements in a plane. The technique does require the presence of certain species which can be an issue as, for instance, NO is consumed in rich hydrocarbon flames and it can, therefore, not be used to measure temperature in the product region of these flames.

TLAF can use the spectral shape of laser-induced atomic fluorescence to de-

---

[13] ± 4-5% of the absolute temperature at low temperatures, +/-50 K at near 1200 K [72].

termine temperature. The atomic species used for this is generally seeded into the flame, but only trace amounts are necessary[76], so the effect on the flame is small or negligible. It does however add the need for seeding, which requires burners designed for seeding, and could be difficult to implement when studying the combustion of solids.

For LITGS a short pulse laser[14] is used to induce a thermal grating, and the reflection from this grating is recorded as a function of time. The signal from this is a decay curve overlaid with oscillations that depend on the speed of sound in the gas. This is in turn related to temperature, and if the gas composition is known, the oscillation frequency can be used to determine temperature. In contrast to a number of other detection techniques, which suffer from collision quenching, LITGS depend on collisions for its signal, and therefore perform very well at high pressures, though less so at low pressure.

4.8 Waterline Thermometry

The use of mid-IR waterlines for temperature determination first described in [81] relies on a group of three resolvable water transition lines structures, here referred to as lines I, II and III, which are shown in Figure 4.8a. These lines lie in the range 3230-3231.6 cm^{-1}, consisting of several individual transition lines. Line group II consist of lines e and f, at 3230.98297 and 3230.98329 cm^{-1}, and line group III, consist mainly of lines g and h at 3231.3206 and 3231.3316 cm^{-1}, with a third peak (i) contributing, but at an order of magnitude lower line strength. The structures are close enough together that they can easily be contained in one scan of a tunable laser, and are also within the bandwidth of the upconversion detector at a set temperature of the periodically poled lithium niobate (PPLN) crystal, which means they can easily be measured together. However, the lower energy level of the transition lines of II is 1789.0428 cm^{-1} with the upper levels at 5020.0261 cm^{-1}, while the lines of III have lower levels at 5035.1265 cm^{-1} and 5713.2500 cm^{-1}, respectively[7]. The upper level of the transitions in group II will therefore begin to populate at the same temperature where the lower levels of group III are populated. This means that in the 1000-2000 K range, which is of particular interest for combustion research, the linestrengths of the lines in group II change little, while the linestrengths of the lines in group III increase rapidly with temperature, as shown in Figure 4.8b. The relative strength of the two features will therefore change rapidly in the temperature interval 1000-2000 K, and the ratio between the two can be used to

---

[14] Generally ns-time scale pulse duration.

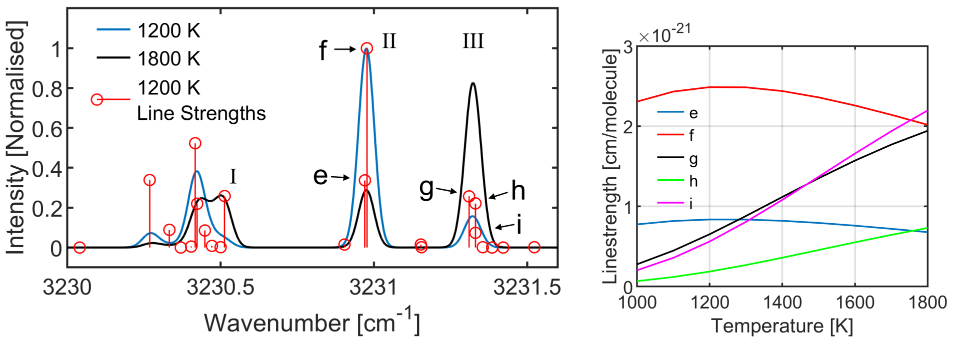

(a) Calculated DFWM signal for the waterlines used for WALTHER, with the individual line positions and strength overlaid. Both the DFWM signal have been normalised using the maximum value for the 1200 K signal, so the relative strength is preserved.

(b) Linestrengths of the individual lines constituting group II (e,f) and III (g,h,i), as a function of temperature.

Figure 4.8

determine the temperature. The shape of structure I is temperature dependent and could be used as an additional fitting parameter.

Although first shown using DFWM, these transition lines can also be probed with other techniques, for instance IPRS[27]. This technique was used for the temperature measurements in both Paper I and III, with IRPS and DFWM respectively. The advantages of waterline thermometry (WALTHER) are: i) the transition lines involved are hot lines, which means there are negligible absorption of the laser outside of the measurement volume. ii) the absorption in the hot gas is fairly weak, which means reabsorption of the signal is not an issue.

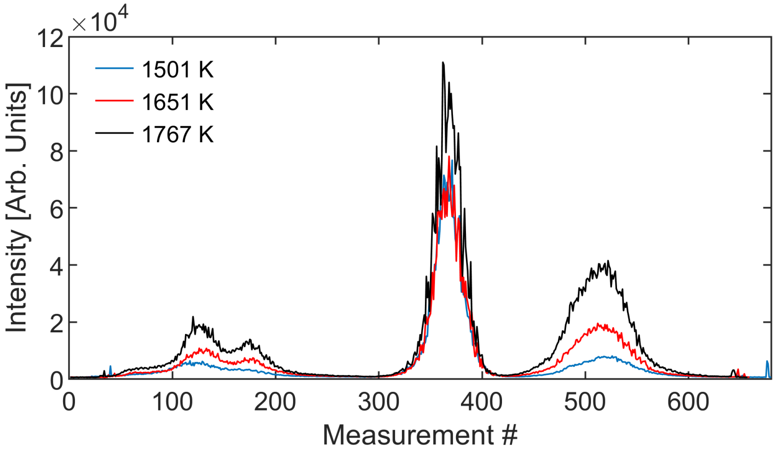

Figure 4.9: Averaged DFWM scans over the range 3230.2-3231.7 cm^{-1} at $I_{pump} = 0.6$ TWm^{-2}. The results shown here are the average of five scans.

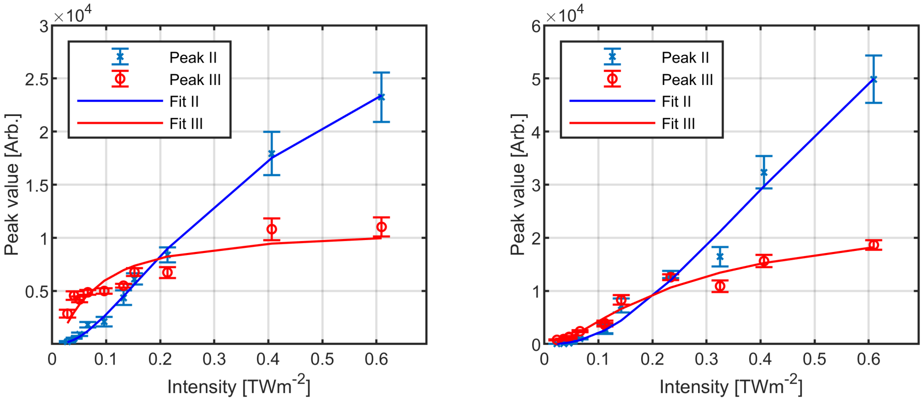

(a) Saturation curves for 1744 K. Saturation intensity from fitting: $I_{sat,II} = 0.62$ TWm^{-2}, $I_{sat,III} = 88$ GWm^{-2}. The maximum intensity, 0.61 TW/m^2, corresponds to a pump pulse energy of 0.22 mJ for each pump beam. The pulse energy at the laser output was 6.0 mJ.

(b) Saturation curves for 1522 K. Saturation intensity from fitting: $I_{sat,II} = 1.48$ TWm^{-2}, $I_{sat,III} = 0.334$ TWm^{-2}. The maximum intensity, 0.61 TW/m^2, corresponds to a pump pulse energy of 0.22 mJ for each pump beam. The pulse energy at the laser output was 6.0 mJ.

Figure 4.10

iii) the range where the relative intensity changes most drastically, and therefore where the technique is most sensitive, matches the temperature range of interest for our flame measurements. When using IRPS or DFWM to perform quantitative measurements, a major advantage of using these waterlines for temperature measurement is that the temperature measurement can be performed with the experimental setup already in place, This not only reduces the time and material needed, but also makes it simpler to ensure that flame conditions are the same for the concentration and the temperature measurement.

The signal from these line groups have been collected in two ways. For systems that do not change in time we scan across the line groups. Multiple scans are performed under the same conditions to obtain averaged scans, such as the ones shown in Figure 4.9. This ensures that we collect signal from the peak of the group, and allow us to use the line integrated signal instead of the peak signal, if that provides a better signal-to-noise ratio. In addition, the line shapes are also recorded, which provide extra information about signal saturation. The alternative to this is to set the wavelength of the laser to the center wavelength of each group and measure the signal directly at the peak. The advantage to this is that allows WALTHER to be used on systems that change on time-scales that are shorter than the duration of a scan[15]. The disadvantage is that requires

---

[15] This is for instance the case for the degassing straw pellets investigated in Paper III. Their volatile phase last approximately 80 s. In this time it is at most, by compromising scan range and resolution, possible to get three scans completed, which is not enough to resolve the

high reproducibility of the wavelength of the laser, and it is difficult to verify whether this is achieved.

The main challenge of WALTHER is accurately converting the measured line ratio to a temperature. When describing the signal from a single line or line group, Equation 4.26 is used to predict how the signal changes with temperature. As the ratio measurement is purely a relative measurement of two signals, it would be tempting to think that the signal of each peak, and thus the ratio could be calculated using Equation 4.26 directly from HITRAN or HITEMP data. However, Equation 4.26 does not include saturation effects, which greatly influence the measured ratio.

A series of measurements were performed, to investigate the importance of saturation effects for WALTHER. 8 $H_2/CH_4/O_2/N_2$ flames, with a known recombination zone temperature, were prepared. DFWM scans were measured across groups II and III In the recombination zone of these flames, for different pump pulse intensities. Saturation curves for the two peak signal of each line group are shown in Figures 4.10a and 4.10b for 1744 K and 1522 K, respectively. This clearly shows that the measured ratio will to a large degree depend on the pump intensity. A fit was made to each measurement series using Equation 4.20, assuming $\delta = 0$ and $I_{pump} \approx I_{probe}$, to obtain values for I_{sat}[16]. The value of I_{sat}, Equation 4.21, depends on the population and coherence relaxation times, τ_1 and τ_2, and on the transition dipole moment, μ. τ_2 is generally determined by the collision rate[32], which explains the temperature dependence of I_{sat}. The difference in the I_{sat} for the two groups at the same temperature can be explained by a difference in μ for each line. To accurately determine temperature from the ratio, it would necessary to either include the saturation in the calculation of the expected signal, or to perform calibration measurements at the pump intensity used for the thermometry measurements.

For practical measurements, we want to use pump energies near saturation intensity to maximize the generated signal and to reduce the effect of collisions. Currently, 6.3 mJ per pulse is the highest energy the dye laser system can achieve in the range of the water line groups. Measurements of the waterline ratio were performed in the 8 flames of known temperature, at 6.3 mJ per pulse, using both scanning and the online approach. The results of both methods are shown in Figure 4.11, together with the ratio calculated from HITEMP 2010 data, without taking saturation effects into account. A 2^{nd} degree polynomial fit has been made to each measurement series, to easily compare the trend of the

---

concentration change sufficiently.

[16] Using Equation 4.20 is an approximation, as it is derived assuming a single isolated transition line, but it is accurate enough for the discussion here.

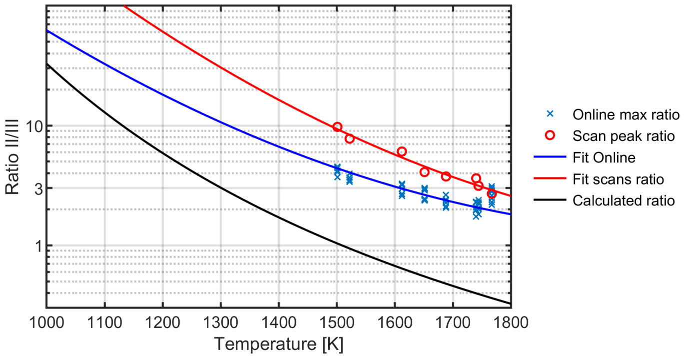

Figure 4.11: Water line ratios measured with the online method and by scanning across the lines compared with ratio predicted from HITEMP 2010 data. 2^{nd} degree polynomial fits have been made to easily compare the trends of each dataset.

measurements and the calculated ratio. Both approaches show a predictable, reproducible trend that could be used for temperature measurements, if a calibration curve was measured. An exception to this is the online values measured for 1767 K, which do not follow the trend of the other online measurements, but we currently have no good explanation of why this is the case. It is also surprising that the online measurements do not follow the same slope as the predicted ratio or the scan ratio. This could be because the wavelength of the laser was not placed at the center of each line group. However, these measurements were performed under stable conditions, and great care was taken to accurately set the laser wavelength, so this seems an unlikely explanation. The reason for the difference between the online ratio measurements and the ratio measured by scanning is so far unclear.

I have attempted to quantify the uncertainty of each method. This has been done by using the fits shown in Figure 4.11 to calculate the temperature for each ratio measurement. The error is then difference between the calculated temperature and the actual temperature of the flame. The online measurements at 1767 K was not included in this calculation. The maximum error was 34 K and 83 K, for scanning and online measurements respectively, and the mean error was 17 K and 30 K. From these error values both methods seem to be useful techniques for thermometry, and I have full confidence that accurate temperature measurements can be performed using scanning with calibration. For the online approach I would not fully trust temperature measurements recorded this way, before a reproducible calibration curve, without outliers, like the ones at 1767 K, have been demonstrated. In this case, WALTHER is still sensitive to the energy and mode stability of the pump laser used for DFWM or IRPS, which

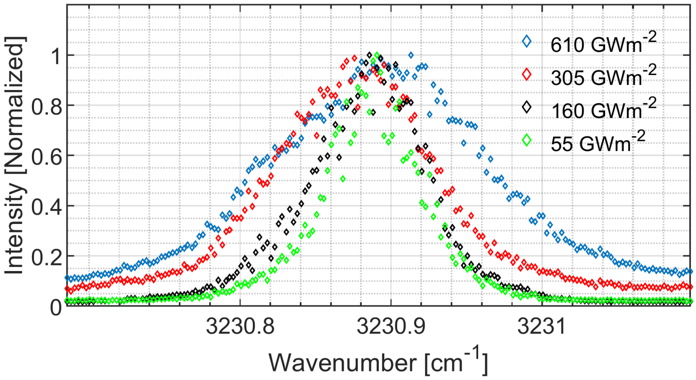

Figure 4.12: DFWM signal recorded for line group III for different pump intensities. The effect of saturation broadening increases the width from 0.6 cm^{-1} to 1.5 cm^{-1} at the highest pump intensity.

can be an issue as described in Chapter 6.

Sun *et al.*[81] used HITEMP 2000 data over HITEMP 2010 data, because it provided a better fit to their experimental results. In particular, lines g and h are spaced further apart according to HITEMP 2000. This results in a broader calculated linewidth for line group III, which matched the width of line group III observed by Sun *et al.*. However, we measured the shape of group III for different pump intensities with the results shown in Figure 4.12. This shows that line group III is much narrower at low pump intensities, which match the width predicted by the HITEMP 2010 data for no saturation. This indicates that the line positions in HITEMP 2010 are more accurate, and the observed broad shape of line group III is the result of saturation broadening rather than the positions of the individual transitions.

Chapter 5

Upconversion

Upconversion detection is the technique of using sum frequency generation to shift an optical signal from longer wavelengths to shorter wavelengths to facilitate detection in the visible or near IR. The main advantage of this is that it allows the use of silicon based detectors, which are generally cheaper, faster, and more sensitive than their mid-IR counterparts. An added advantage is that the upconversion process has a narrow angular acceptance and a narrow bandwidth, approximately 6 cm^{-1} for the work presented here, which greatly reduces the impact of thermal background radiation. These factors combined generally more than compensates for the loss in the conversion process. These advantages were discussed already in 1968[82], but due to technical limitation at the time the practical uses were limited. The field lay dormant for a long period, during which the development of cheap and powerful laser diodes (LD) and the advances in the production of nonlinear crystals, especially PPLN, opened new possibilities. The field saw renewed interest when highly efficient intracavity upconversion was demonstrated[83]. During the last decade the field of upconversion detection has spread out to cover several different sub-areas, that each focus on utilizing different advantages of the upconversion process, namely hyperspectral imaging, lidar applications, short time scale physics and single-photon detection.

There is significant interest in achieving hyperspectral imaging, especially in the medical field for characterizing tissue samples for diagnostics[84]. Upconversion has proven itself a powerful tool here, as the angle dependence of the phase-match allow for simultaneous upconversion of a broad wavelength range[85, 83]. This was demonstrated early on using PPLN[86, 87], however the acquisition rate was at first fairly low. This has been adressed by the use of higher brightness sources[88], which allow upconversion systems with expanded fields of view, which in turn lowers the time to acquire a full image[89, 90]. However, the infrared features useful for diagnostic purposes mostly lie at wavelengths of 6 µm and above, which is outside the transparency range of lithium niobate. Efforts have therefore been made to extend the technique to nonlinear materials capable of working with longer wavelengths, in particular aluminium gallium sulfide (AGS). Hyperspectral imaging have been demonstrated for the 6-8 µm range[91], with a spatial resolution of 70 µm. A narrow linewidth scanning system has been demonstrated at 10 µm[92], which was then used for hyperspectral imaging using rasterscanning[93].

With the continued issue of global warming looming, there is both an interest in and a need for accurate atmospheric measurements of greenhouse gasses. Most of these gasses do not have features in the visible or near infrared range, which is why infrared lidar is used for this. The low noise, fast detection and high background discrimination of upconversion detection can improve the sensitivity of these measurements, and this has been shown for the detection of both CO_2 and CH_4 using an intracavity setup[94, 95]. Sensitive detection of CH_4 using light scattered from a solid target has also been shown demonstrated a self-gating pump setup[96]. Because the lidar signal does not require transverse spatial information to be preserved, the upconversion process can be done in a waveguide[97]. The increased confinement makes it possible to reach higher conversion efficiencies, but adds coupling losses.

Parametric conversion has a time response in the sub-ps range. This makes it possible to shift mid-IR signals to the near-IR range without distorting their temporal structure. The faster detectors in the near-IR allow measurements with ns-resolution, which has been used for pulse characterization of supercontinuum lasers[98] and for photoluminescence spectroscopy in the mid-IR[99]. Alternatively, the upconversion process can be used to time gate the signal, by using a short pump pulse. As upconversion only takes place for the duration of the pump pulse, this can be used to provide picosecond time gating to IR imaging[100, 101]. In addition to the short time response, the phase and spectral modulation is maintained through the conversion process. A broadband conversion scheme was developed[85], capable of conversion over the entire 3.6 to 4.85 µm range, without sacrificing too much conversion efficiency for conversion range. This made it possible to employ upconversion detection in conjuntion with mid-IR optical coherence tomography[102].

The strong background suppression of the upconversion process is a step towards efficient mid-IR single photon detection. This was already demonstrated in [83], but has since been shown for waveguide upconversion as well[97, 103]. The role of

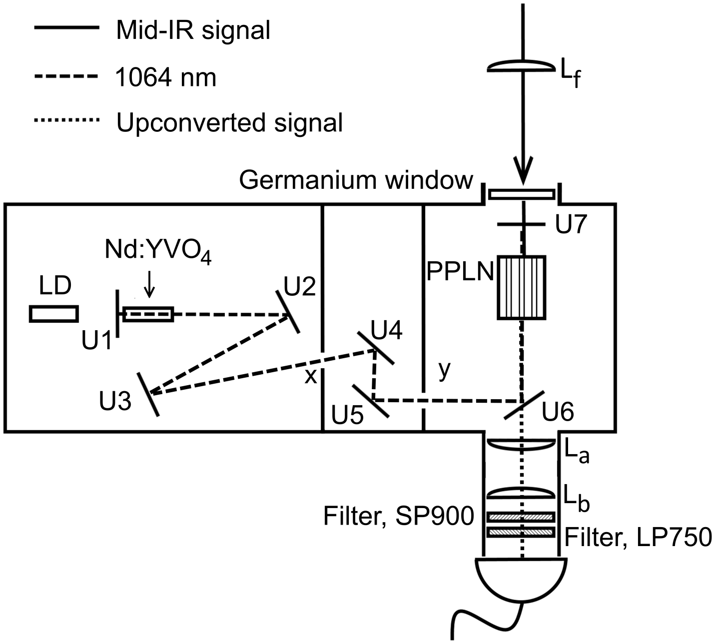

Figure 5.1: LD: laser diode pump. U1-7: Upconversion cavity mirrors, except for U1 and U3, they are all plane. Lenses L_a and L_b are used to image the upconverted signal onto a point on the detector. Lens L_f is used to focus the mid-IR signal to a spot size matching the intracavity field.

this technique in quantum optical applications was then established, when it was demonstrated to work well for single photon pair coincidence measurements[104].

Before the start of the work presented here, upconversion was shown to greatly increase the sensitivity of the DFWM setup in Lund[105]. In Paper II, upconversion was combined with IRPS to investigate whether a similar improvement could be achieved for IRPS. The implementation of upconversion detection was shown to improve the sensitivity by a factor of 8, which, while a significant improvement, was not as great as the improvement seen for DFWM. This is because the sensitivity of the IRPS setup is limited by the extinction ratio of the polariser set. As the combination of DFWM and upconversion seemed most promising, this was used in Paper III, which enabled the quantitative detection of HCN in a flame environment down to a few hundred ppm.

5.1 Upconversion Detector

A diagram of the upconversion detector used for the work presented in this thesis is shown in Figure 5.1. The basic idea of this setup is to achieve a high intensity pump field, without using a very powerful laser, by placing the nonlinear crystal inside a high finesse cavity. In this setup a PPLN crystal is used as the nonlinear material. The cavity consists of mirrors U1-U7. A Nd:YVO$_4$ crystal is used as the gain medium for the 1064 nm pump field. The laser crystal is pumped using a 3 W, 880 nm laser diode, LD. The cavity mirrors are coated to be transmissive for 880 nm. This, together with the baffle[1] between the laser crystal compartment and the PPLN compartment keeps any stray LD light or flourescence from the Nd:YVO$_4$ crystal from reaching the detector as noise. Long and short pass filters are placed in the detector tube to prevent the 1064 nm and the parasitic second harmonic at 532 nm, generated in the PPLN, from reaching the detector. The mid-IR signal is focused by lens L$_f$ into the PPLN to a beamwaist radius of approximately 90 µm, to match the the size of the intracavity field mode. The Germanium window is used to block incoming light in the wavelength region of the upconverted signal, to ensure that the signal seen on the detector is upconverted and not background from ambient light. The standard detector used with the upconversion module is a UI-5240CP-NIR-GL camera from IDS.

The work performed during this thesis has been focused on implementing the upconversion detector as a point detector together with techniques that do not generate any spatial structure to the signal that must be measured. The reason for using a camera instead of a point detector for measuring the upconverted signal is mostly a practical one, the camera chip is 6 mm x 5 mm, making alignment trivial compared to point detectors with active areas of 1x1 mm or less. The large size of the camera makes it easy to find the signal, and the few pixels containing the signal can then be selected, so that only the intensity detected on those is recorded. In addition, we have found that it is not the sensitivity of the camera that is the limiting factor for the detection sensitivity, but the background noise associated with the IRPS and DFWM setups.

The conversion efficiency will vary slightly from alignment to alignment, but the theoretical maximum for the photon-to-photon efficiency, calculated from Equation 4.9, lies in the range 9-13 %, as shown in Figure 5.2. For Paper V it was measured to be 6.0%, which is what can be reasonably expected when taking into account losses in optics and imperfections in alignment. The conversion efficiency has likely been lower for the work performed using the dye laser for

---

[1] This consists of holes x, y, and mirrors U4 and U5.

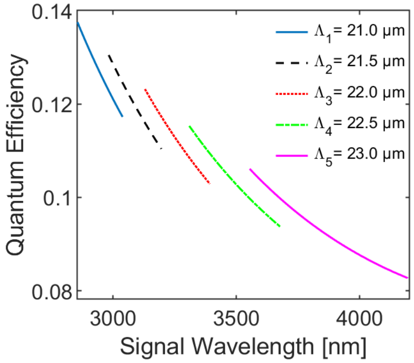

Figure 5.2: Theoretical maximum quantum efficiency of the upconversion module shown as a function of phasematched wavelength for the available poling periods.

signal generation, because the mode of the HeNe laser used for Paper V was much closer to a fundamental Gaussian than the mode of the IR dye laser setup.

Using quasi-phasematching in PPLN, it is possible to always use the highest nonlinear tensor element, d_{33}, which requires type-IV[2] phasematching. This means that ω_{IR}, ω_P, and ω_{up} are all polarized along the extraordinary crystal axis. The crystal used for the upconversion detector was designed to allow phasematch of any wavelengths in the interval 2860 nm to 5500 nm. This requires channels with poling periods 21.0 µm, 21.5 µm, 22.0 µm, 22.5 µm, and 23.0 µm. The poling period determines the wavelength range that can be phasematched, and temperature tuning is then used within that range. Sellmeier coefficients from

---

[2] All fields are polarised along the extraordinary axis.

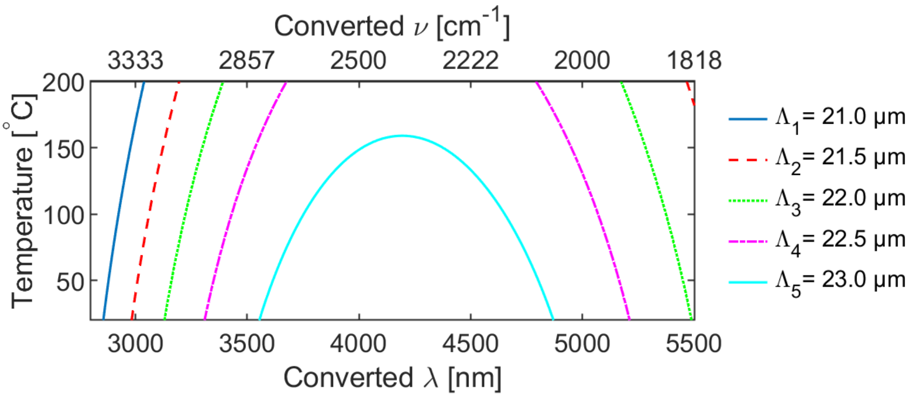

Figure 5.3: Phasematch curves for the upconversion detector, for the poling periods channels available in the PPLN crystal.

[106] were used together with Equation 4.8 to calculate phasematch curves, as a function of temperature, for the crystal. These are shown in Figure 5.3.

While a number of features were implemented in the upconversion detector to reduce background noise, there are still two sources of background noise associated with the upconversion stage. As have been described briefly in Paper V, and in detail in [107] and [108], these are spontaneous parametric down-conversion (SPDC) and thermal emission from the PPLN crystal. The SPDC dominates below 3.5 µm and the thermal noise dominates above 3.5 µm. In Paper V these sources were measured to an average power of approximately 100 fW at 6% conversion efficiency[3], depending on poling period, wavelength and crystal temperature. Both also have a strong angle dependence[107, 108], which could be an issue if the detector is used to record a broadband spectrum with a weak source[109].

The SPDC and thermal noise limit the sensitivity for long term continuous measurements, but most of the work performed during this thesis has used a pulsed ns-laser to generate the signal. This means the detector can be time-gated to a very short interval, which reduces the influence of the continuous noise sources to a level where they are negligible. The limiting factor for detection sensitivity instead becomes specific to each technique. The limiting factor for IRPS is the extinction ratio of the two polarisers. The extinction ratio is 7 orders of magnitude, and the bleed through of the probe beam shows up as background noise, which limits the detection sensitivity. For DFWM the limiting factor is the background arising from light scattered from the beamblock used to block the signal beam.

---

[3] For a point detection setup

Chapter 6

Noise

When discussing noise here, we will divide it into two sub groups: background noise, which is the noise signal generated on the detector from sources other than the real signal we wish to detect; and signal variation, which is variations in the intensity of the signal itself from sources other than the concentration variations we wish to measure. In our case, the signal variation arises mainly from the stability of the pulse energy and mode structure of the laser generating the signal, which will be discussed further in Section 6.1. This chapter will deal mainly with the characterization of noise sources inherent to the upconversion detector. Background noise specific to a certain detection method will be dealt with elsewhere, although the general theory presented here will also apply to those.

In general, noise equivalent power, NEP, can be used to compare the sensitivity of detectors of different bandwidth:

$$\mathrm{NEP} = \frac{\sigma_b}{p_r\sqrt{B}} \tag{6.1}$$

where σ_b is the standard deviation of the background output of the photodetector, B is the bandwidth of the detector, and p_r is the power response of the detector, which is defined as the voltage response generated per unit of optical power incident on the detector:

$$p_r = \frac{\bar{x}_s - \bar{x}_b}{P_{opt}} \tag{6.2}$$

where $\bar{x}_b$ is the mean background, $\bar{x}_s$ is the mean signal, and P_{opt} is the optical power incident on the detector. Equation 6.1 is appropriate when operating in the regime above single photon counting. For the regime where the signal is measured in counts instead of a continuous variable, the NEP can be found by[110, 111, 112]:

$$\mathrm{NEP} = \frac{E_{ph}\sqrt{2RBC}}{\eta} \tag{6.3}$$

where E_{ph} is the energy of a single photon, RBC is dark counts per second, and η is the detection efficiency.

One of the two main sources of background noise for the upconversion detector is spontaneous parametric down-conversion (SPDC). This noise is generated when a pump photon spontaneously decay into two photons at longer wavelengths in the PPLN. This is not a phasematched process, and in an ideal periodically poled crystal it would not occur. However, in practice there are random errors in the size of each poling period domain[113], which makes it possible for this process to happen. The problem occurs when the photons generated through this process are at the same wavelength as the infrared signal, as they will then be phasematched and upconverted in the same way as the signal. The resulting upconverted noise photons are indistinguishable from the signal both spectrally and, to a certain degree, spatially. The upconverted SPDC noise have been shown to have an angular dependency[107], but the noise at the exact same wavelength as the signal will be at the same position. The angle dependence of the rest of the noise depends on the specific crystal, which makes it difficult to make a spatial filter which works reliably. This is the dominating noise source inherent to the upconversion detector below 3.5 µm.

The second main source of background noise for the upconversion detector is thermal noise. This is not an issue in the spectral region where the PPLN crystal is most transparent, but for wavelengths above 3.5 µm the PPLN crystal begins to have absorption features, which of course also means that it emits radiation at these wavelengths. The thermal noise increases in intensity, if the PPLN is raised in temperature to achieve phasematch, as would be expected from Kirchhoff's black body radiation law.

6.1 Reference Beam for IRPS

While background noise is the limiting factor for the lowest concentration that can be measured, the signal variation is one of the two main contributors to the uncertainty of any concentration measurement[1]. The two main reasons different

---

[1] The other source of uncertainty is uncertainty on temperature measurement, as the signal strength depends exponentially on the temperature, see Chapter 4.

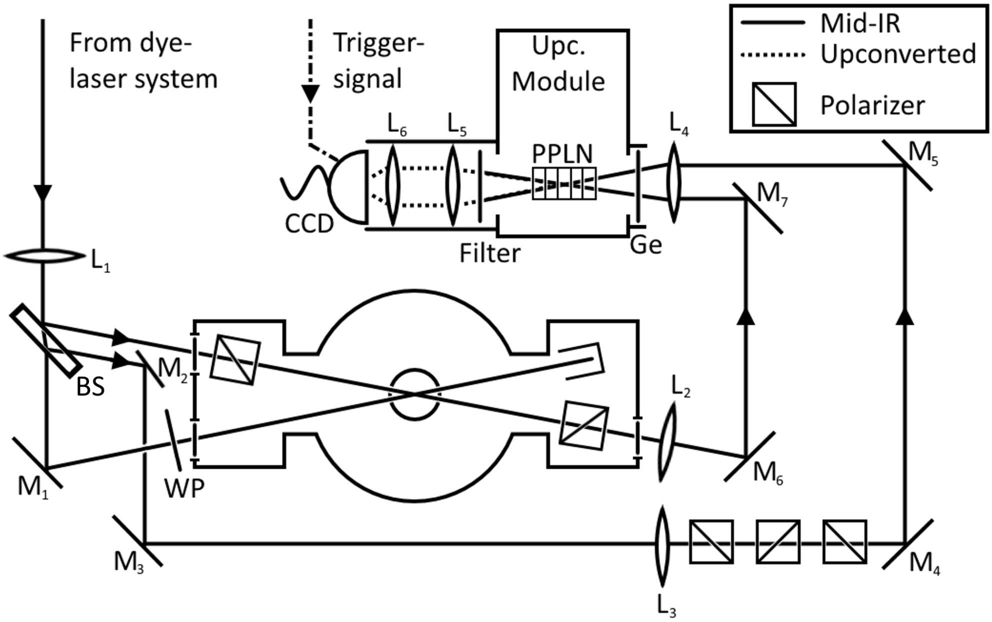

Figure 6.1: Diagram of the reference beam implementation for the IRPS setup. Mirror M_1 is a semiconductor mirror coated for the mid-IR. M_2-M_7 are protected gold mirrors. BS: beam-splitter, here is used a CaF_2 window. WP: waveplate. L_1-L_4 are lenses of focal lengths 1000 mm, 500 mm, 500 mm, and 100 mm, respectively.

signal intensities are generated for the same concentrations when using DFWM or IRPS are variations in the pulse energy, or variations in the spectral mode structure of the pulses delivered by the mid-IR pulsed dye laser.

To compensate for the variation in pulse energy, a reference beam system was implemented for the IRPS system, to evaluate whether the signal variation could be reduced significantly by taking the variation in pulse energy into the calculations. This was done as shown in the diagram in Figure 6.1. The back reflection from the CaF_2 window, used to separate the probe beam from the pump beam, was used as a reference beam. This was then reduced in power using three polarisers placed in series. Both the signal beam and the reference beam were then focused into the upconversion module at an angle, using the angular dependency of the phasematch condition, described in Chapter 5, to detect both signal and reference beam simultaneously at different positions on the camera chip.

The polarisers were opened slightly, and the laser was kept at a set wavelength. The signal and reference beam were recorded together for 4 minutes. The measured intensities are shown together in Figure 6.2a and their correlation is shown in Figure 6.2b. For these conditions, the two show a high degree of correlation.

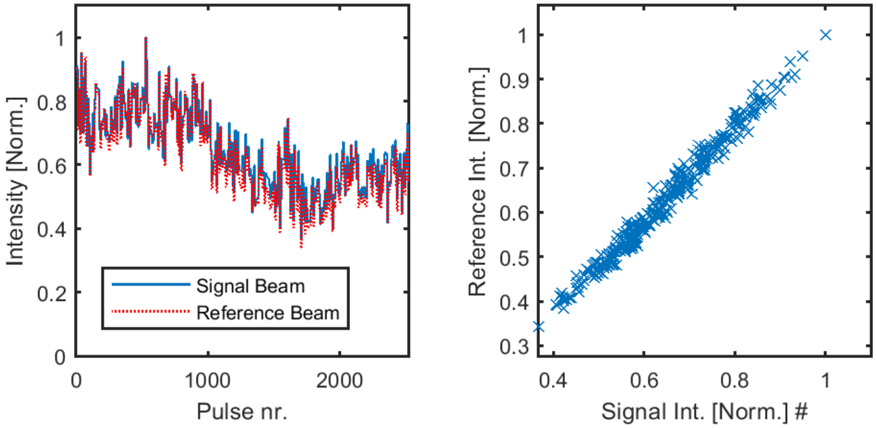

(a) Signal and reference beam shown together, for the polarisers slightly open, and the laser at a set wavelength.

(b) The correlation of the two signals shown in Figure 6.2a.

Figure 6.2

For most measurements, the IR laser will not be kept at a set wavelength, but will be scanned across an absorption line. To investigate the performance of the reference beam during scanning, the laser was scanned over the interval 3138-3140 cm^{-1}. The recorded intensities and their correlation are shown in Figures 6.3a and 6.3b. In this case, the two beams show a lower degree of

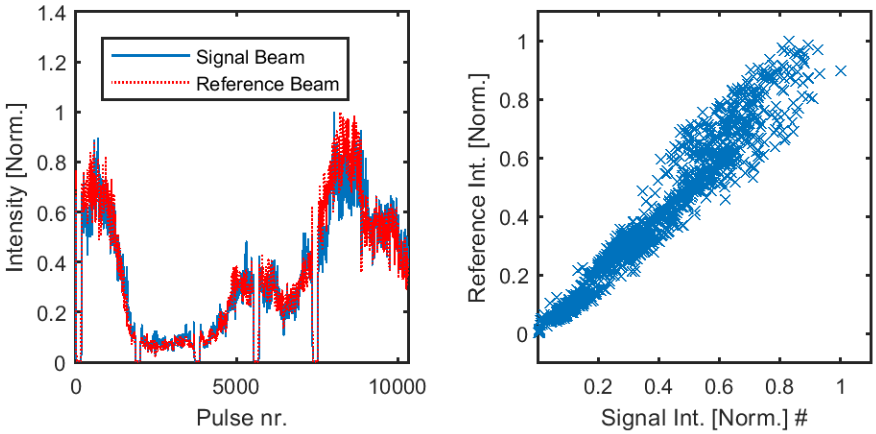

(a) Signal and reference beam shown together. The laser is scanned over the interval 3138-3140 cm^{-1} five times. The signal is shown with solid blue, the reference is the dashed line.

(b) The correlation of the two signals shown in Figure 6.3b.

Figure 6.3

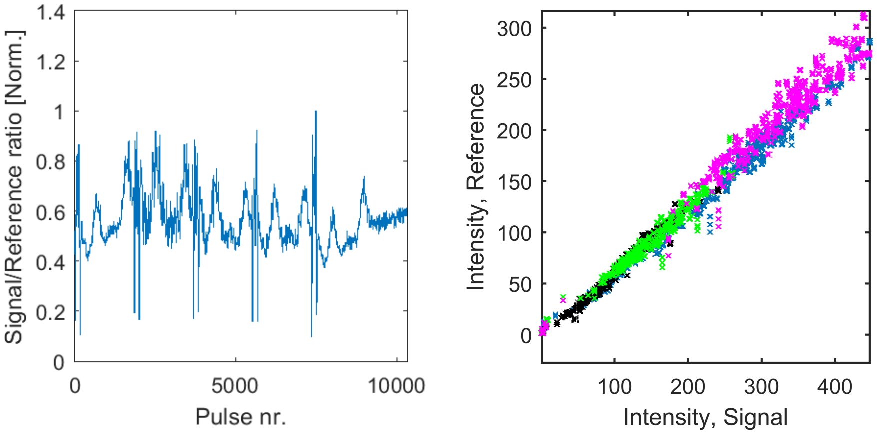

(a) The ratio between the signal and reference beam is not independent of wavelength. Here is shown the reproducible ratio between the two for the five scans over the interval 3138-3140 cm^{-1} shown in Figure 6.3a.

(b) The correlation of the two signals shown in Figure 6.3a, but taking into account the wavelength dependence shown in Figure 6.4a. Each colour represents a separate scan.

Figure 6.4

correlation than for a set wavelength. Figure 6.4a shows how the ratio between the signal and the reference beam varies during the five scans, and this explains the poorer correlation. However, The ratio shows a similar structure for each scan, which indicates that the ratio between the two is not constant, but changes as a function of wavelength. If this structure is averaged and divided out before calculating the correlation, the two signals show a higher degree of correlation, which is shown in Figure 6.4b.

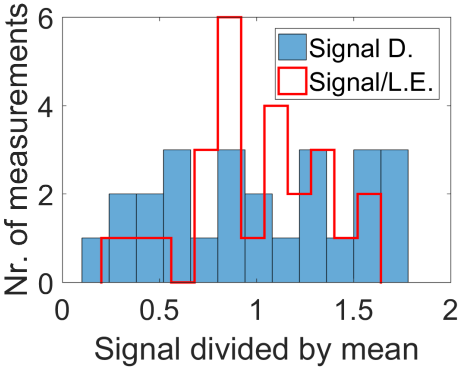

Figure 6.5: Histogram showing the distrubution with and without taking the variation of the pulse energy into account. The value of each measurement is the integrated signal of the R(13) line of the v_3 band of CH_4. "Signal D." is the signal measured directly, and "Signal/L.E." is the signal divided by the laser energy.

A flow of 180 ppm CH_4 in N_2 was prepared to serve as a test target for evaluating how much the use of a reference beam could reduce the spread in the signal when measuring a set concentration. Figure 6.5 contains a histogram showing the distribution of the measured signal around the mean, and the distribution of the signal divided by the laser energy for comparison. This shows that recording the pulse energy can be used to reduce the variation, and therefore the uncertainty, of the measured values. For the measurements shown here the standard deviation is reduced by a factor 2, when dividing with the pulse energy.

While reducing the standard deviation with a factor two is an improvement, implementing and maintaining the alignment of the reference beam requires significant time and effort. For experiments where multiple measurements can be made of the same variable under stable conditions, the same reduction in uncertainty might be achieved more reliably by simply repeating the measurement. The reason the implementation of the reference beam did not result in a larger reduction of the signal variation may have been a result of the influence of variations of the spectral mode structure of the pulses. The IR pulses from the dye laser system consist of several longitudinal modes. If their relative strengths change from pulse to pulse, the power of the generated signal will change, due to the change in the overlap with the transition line, even if the overall pulse energy is constant. To address this problem we attempted to build an optical parametric generator with amplification, which is described in Chapter 7, as an alternative IR source to replace or supplement the dye laser system. The dye laser system has, however, been upgraded with a dynamic modulation operation system, which might address the original issue, but systematic measurements of the signal stability has not yet been performed with the dye laser after the upgrade.

Chapter 7

Lasers

7.1 Introduction

When performing nonlinear spectroscopy it is advantageous to have a light source with high brightness, possibly pulsed to provide time gating, and ideally a narrow linewidth with tunability. Lasers are used, because they are the only light sources capable of providing all these characteristics.

A laser fundamentally consists of three parts: a gain medium, a pump, and a feedback mechanism. The gain medium must have an energy level structure that allows the pumping of an optical transition, usually in a three or four level scheme[9]. The pump is necessary to provide the energy to shift the gain medium to the higher energy level in the optical transition, this can be done optically, by using, for instance, another laser or flash lamps, or it can be done electronically, by running a current through the gain medium. Thirdly, it requires a feedback mechanism, to ensure the emitted light is amplified by stimulated emission. Controlling the feedback mechanism gives spatial and spectral control over which of the spontaneously emitted light is amplified.

7.2 Quantum Cascade Lasers

A quantum cascade laser (QCL) is very similar to a laser diode. Both are semiconductor structures built to have an active optical region that can be pumped electronically and emit within the desired wavelength range, and both use quantum wells to design the energy level structure. The difference is that

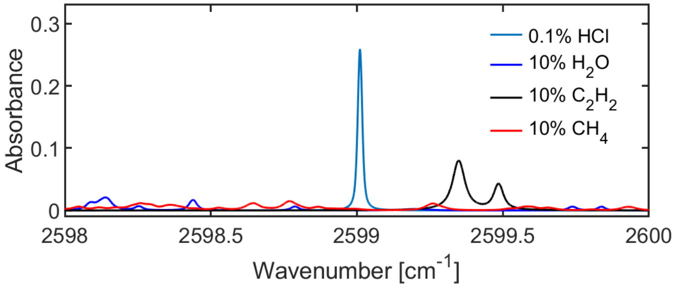

Figure 7.1: Spectra of the $v_1(0 \rightarrow 1)$, P(12) transition line of HCl and molecular species with nearby transition lines at 1500 K.

in regular laser diodes the optical transition is between the conduction band and the valence band, whereas in a QCL the optical transition is between two energy levels in the same quantum well. Because these energy transitions are small compared to the interband transitions, it is possible to construct multiple quantum wells in a series, where an electron in the lower energy level of the first quantum well can tunnel into the upper level of the optical transition in the next quantum well. Ideally, the electrons will then cascade from quantum well to quantum well and emit a photon for each quantum well, yielding several photons for each electron-hole pair. The advantage of this design is that it allows much lower energy differences between the upper and lower levels of the optical transition than regular diodes, which in turn makes it possible to build semiconductor laser in the mid- and far-IR. The downside is that because the design is more complicated it is more sensitive to production errors, and as the upper state lifetime is in the ps-range they need to be pumped with high

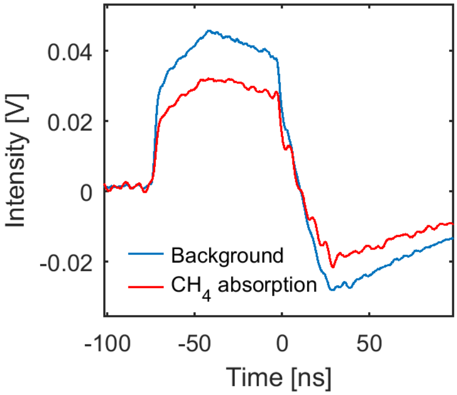

Figure 7.2: Absorption with the QCL in CH_4/N_2 mix near 2600 cm^{-1}.

currents. For this reason they are usually pulsed, to allow time for cooling.

In the IR-group in Lund, there is an interest in monitoring HCl with high sensitivity, and we had identified a HCl transition-line in the fundamental band, see Figure 7.1, that could perhaps provide a stronger signal with less interference than the transition lines near 1750 nm, which have previously been used in our group. Through the Mid-Tech project we had the opportunity to work closely with J. Tomko from the group at Humbolt University lead by W. Masselink, who where capable of designing and producing QCLs. They produced a QCL to match the wavelength of the HCl line, with an external cavity setup for tuning and narrowing of the line-width.

We attempted to characterize the QCL by measuring an absorption spectrum of CH_4 peaks in the range 2595-2605 1/cm, as we lacked a spectrometer or wavemeter covering the appropriate wavelength range. It was possible to observe the absorption of the group of transition lines, however we found that the linewidth was too broad to resolve the line structure. A possible explanation of the broad linewidth we proposed, was that the heating during pumping caused wavelength tuning, and that the instantaneous linewidth might be narrow, but that the pulse as a whole was not. We, therefore, measured the intensity of a single pulse during absorption,using upconversion in combination with a fast detector. If the instantaneous linewidth was narrow, we would expect to see a strong dip in the pulse as it tuned across the transition line, however, as can be seen in Figure 7.2 this was not the case. While this attempt at improving the sensitivity of HCl detection was unsuccessful, the $v_1(0 \rightarrow 1)$, P(12) HCL line is both strong and relatively free of interference[1], and I would suggest keeping it in mind should an appropriate laser source become available.

7.3 Dye Laser System

The dye laser system, shown in Figure 7.3 is pumped using a flash lamp pumped Nd:YAG laser (Quanta-Ray Pro-290-10). This delivers 1064 nm pulses of 2000 mJ of 8-12 ns duration. It also contains an internal SHG crystal, which allow it to deliver 1000 mJ pulses of 8-12 ns duration at 532 nm. The two wavelengths are separated at the output of the laser, and the 532 nm pulses are used to pump the dye laser section of the system, while the 1064 nm pulses are used to pump the DFG section. The 532 nm pump is split between between three dye cells in the dye laser section, one for the laser cavity, a pre-amplifier and an amplification stage. The dye cells are continuously flushed through with dye

---

[1] As far as I have could determine from the HITRAN data available.

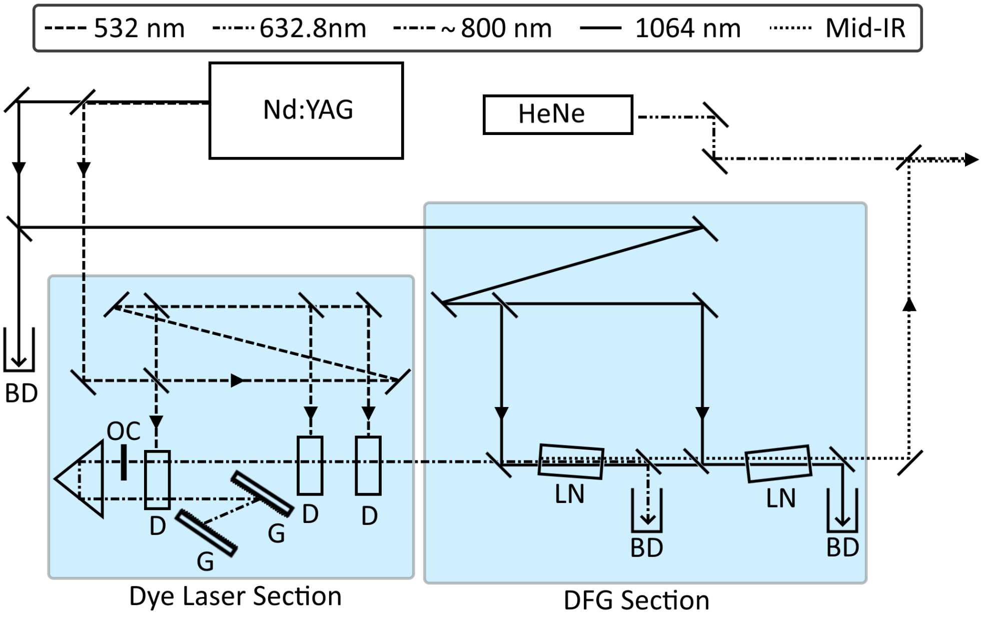

Figure 7.3: Diagram of the dye laser system. G: Grating, D: Dye cell, BD: Beam dump, LN: Lithium niobate crystal. OC: Output coupler

to lessen the impact of dye bleaching and heating. An electronically controlled grating is used to provide tunability within the gain spectrum of a given dye, and the dye can be changed to provide access to different spectral areas. The DFG section contains two stages, a generation stage and an amplification stage. In the first stage the mid-IR pulse is generated using DFG between the 1064 nm beam and the dye laser output. The dye laser beam is then removed with a dichroic mirror, and the mid-IR pulse continues to the second stage, where the mid-IR is amplified using the 1064 nm pump. Both stages use a lithium niobate crystal as the active medium. The remainder of the 1064 nm pump is then removed, and the mid-IR beam is overlappet with a 633 nm beam from a HeNe laser, to simplify alignment. The linewidth of the generated mid-IR pulses is estimated to be less than 0.04 cm^{-1}, with pulse energies in the range of 3-6 mJ per pulse.

The full tuning range of the dye laser is 540-900 nm, which requires changing between several different dyes. For each dye, tuning over the gain region of that dye is done using the grating. The tuning range of the dye laser does not translate directly to tuning range in the IR, as the DFG stage is limited by the cut of the lithium niobate crystals to the range 1.8-3.8 µm.

The dye laser cavity is now equipped with a dynamic modulation system, which vibrates the end mirror to randomize the mode structure. This was installed during 2019, and was therefore only used during the investigation of saturation effects in waterline thermometry.

7.4 Optical Parametric Generator

7.4.1 Introduction

The motivation for building an optical parametric generator was to make an alternative mid-IR source to address the pulse instability, especially found during tuning, of the dye laser system described in Chapter 6. This would then aid in flame measurements by reducing the signal variation. Through the Mid-Tech project we had the opportunity to cooperate with the optical parametric oscillator group at ICFO. In addition, we had access to a high energy pulsed Nd:YAG laser and a large aperture PPLN crystal, that could be used for amplification. We therefore decided to work on a seeded optical parametric generator with an amplification stage, as we had the physical resources and the expertise of our collaborators. Similar systems had also been successfully demonstrated before[114, 115, 116, 117, 118].

7.4.2 Experimental Setup

A diagram of the setup is shown in Figure 7.4. A 4 W average power Nd:YAG laser (Quanta-Ray Lab-130-10) was used as the pump. This was pulsed at 10 Hz, delivering pulses of 400 mJ per pulse. The Nd:YAG laser system included a seeding LD, locked to the laser cavity, in order to narrow the 1064.43 nm laser, and a half-wave plate, to turn the axis of the linearly polarized output. The linewidth of the laser, with injection seeding, is less than 0.003 cm^{-1}. The 1064 pump beam was reduced in power in two stages using polarization selecting beam splitters, the first stage simply reducing the power as much as possible, and the second stage uses an additional half-wave plate to control pulse energies delivered to the PPLN crystal. This reduction in pulse energy was necessary to remain below the PPLN damage threshold. The collimated pump beam diameter was scaled down to 2.5 mm using lenses L_1 and L_2, with focal lengths of 300 mm and -75 mm, respectively. For practical reasons, the waste beam from the second beam dump was reflected out in the horizontal plane, which in turn resulted in the pump beam passing through being horizontally polarized. The polarization of the seed laser diode output was turned using a half-wave plate to

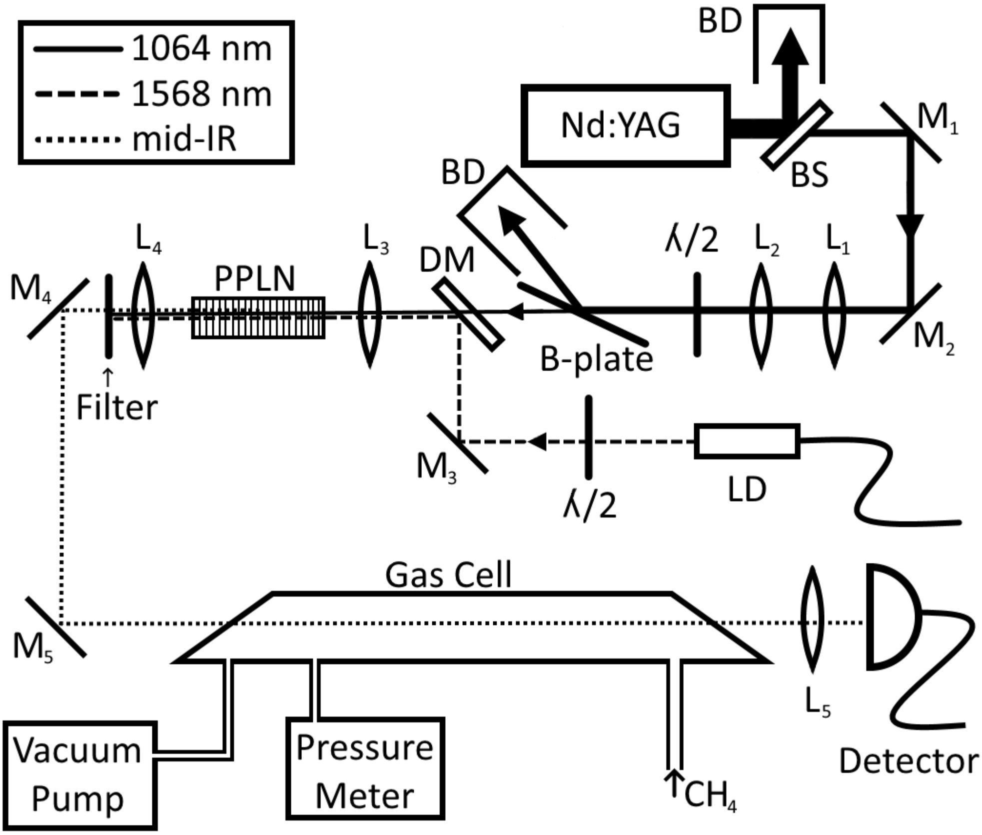

Figure 7.4: Diagram of the OPG and the gas cell used for linewidth characterization. BD: Beam dump. BS: Beam splitter. M$_i$: mirrors. L$_i$: lenses. LD: Laser diode. DM: dichroic mirror. B-plate: Brewster plate, coated for use as a beamsplitter. $\lambda/2$: half-wave plate.

match the polarization of the pump laser, and the PPLN crystal was oriented appropriately for this orientation of the polarization. As this process uses type IV phasematch, the generated mid-IR light was also horizontally polarized. The seed laser used here was a 5 mW continuous wave single mode laser with a 2 MHz linewidth, tunable without modehops in a 2 nm range around 1568.5 nm. The pump and seed laser beams were combined using a dichroic mirror, and lens L$_3$, focal length 150 mm, was used to focus the combined beams down to a beam waist radius of approximately 70 µm. Ideally it would have been better to use a wider beam, but we were limited by the power of the seed laser. When using a wider beam than this, the seed intensity was too low for the seeding to be effective. The PPLN used for the generation stage had an aperture of 2 mm x 1,9 mm, and a length of 50 mm. Both end facets were AR coated for 1064 nm (R<1%), for 1450-1600 nm (R<5%), and 3200-3800 nm (R<1%). The poling period of the crystal was 30.7 µm. The PPLN crystal was kept at 53 °C. After DFG in the PPLN, the generated mid-IR was collimated using lens L_4, and the pump and seed laser was removed with a long pass filter.

The linewidth was determined by measuring a low pressure absorption spectrum of methane. The gas cell is not sealed well enough to maintain pressure throughout the measurement. Therefore, the gas cell was kept at constant pressure by running the vacuum pump with the control valve almost closed, and adjusting the gas flow into the cell to keep the cell at an equilibrium between the gas flow into and out of the cell. This was monitored using a pressuremeter. The signal was then detected using a cryogenically cooled indium antimonide photodetector (Teledyne Judson technologies, J10D-M204-R04M-60), with a bandwidth of approximately 10 kHz.

7.4.3 Characterization of the Generated Light

To better understand the generation process, the intensity of the depleted pump pulses where measured using a 5 GHz InGaAs photodetector (Thorlabs: DET08C). The acquisition was limited by the 1 GHz bandwidth of the oscilloscope (Lecroy Waverunner 6100A). The measurements were performed with the seed LD tuned to 1568.3 nm, Figure 7.5a and 7.5b show the undepleted pump pulse of 140 µJ, together with the depleted pump pulse, with and without seeding with the LD. As can be seen, the depletion is not uniform. Without considering depletion of the pump, the highest conversion would be expected at peak intensity. This is the case for 80 µJ pump pulses, as seen in Figure 7.6a, but for 140 µJ the degree of conversion near peak intensity is limited by back-conversion. The optimal pump pulse energy would be somewhere between 80 µJ and 140 µJ, both for peak conversion efficiency in the center of the pulse, and because the output energy is less sensitive to fluctuations of the pump energy at peak conversion efficiency. In Figure 7.6b the 1568.3 nm output light from the PPLN was measured, with and without seeding. The large increase in pulse intensity demonstrates that the DFG process was seeded successfully.

Controlled tunability of the generated mid-IR was achieved by temperature tuning the seed LD. The connection between the two is shown in Figure 7.7a. The wavelength of the LD was measured using a wavemeter, and the wavelength of the generated mid-IR was calculated through energy conservation between the pump and the seed laser, as described by Equation 4.13. The LD could be tuned in the range 1567.5 nm to 1569.5 nm, with no modehops. This yielded a mid-IR tuning range of 3308.5 nm to 3317.3 nm. The pulse within this range lay between 10-12 µJ, as shown in Figure 7.7b. The mid-IR pulse energy was approximately

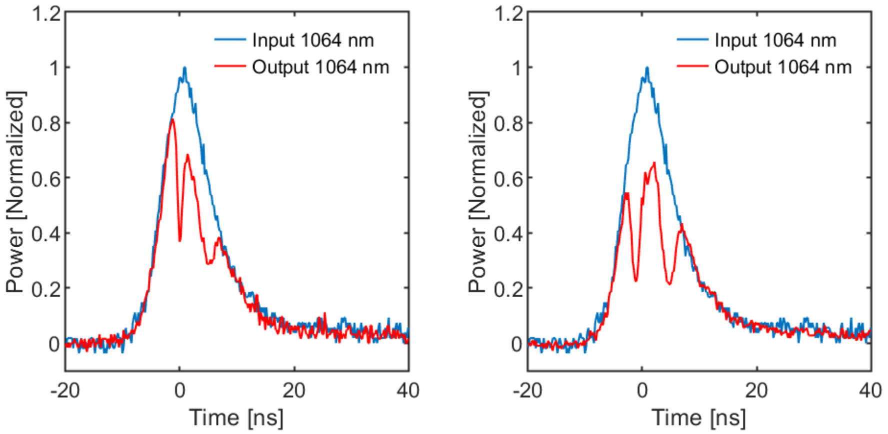

(a) Depletion of the pump pulse with no seeding. The energy of the pump pulse is 140 µJ. FWHM at input is 9.3 ns.

(b) Depletion of the pump pulse with seeding. The energy of the pump pulse is 140 µJ.

Figure 7.5

linear with respect to the pump pulse energy. The mid-IR pulse energy was stable over time; 500 consecutive pulses were measured, which showed a stable mean and standard deviation of 5.3 % of the mean.

One of the main requirements for a laser for nonlinear spectroscopy is a narrow linewidth. The linewidth of the generated mid-IR pulses was therefore measured

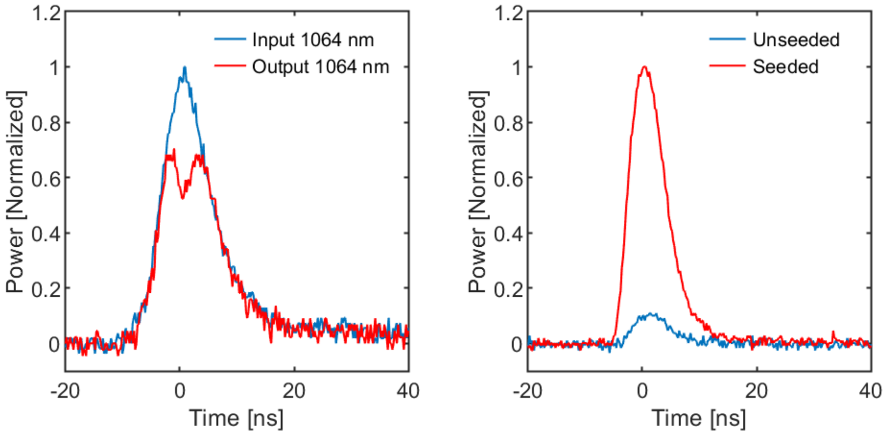

(a) Depletion of the pump pulse with seeding at lower power, the energy of the pump pulse is 80 µJ here.

(b) Power generated at 1568.3 nm. A clear response is seen when seeding the DFG process. The energy of the pump pulse is 140 µJ.

Figure 7.6

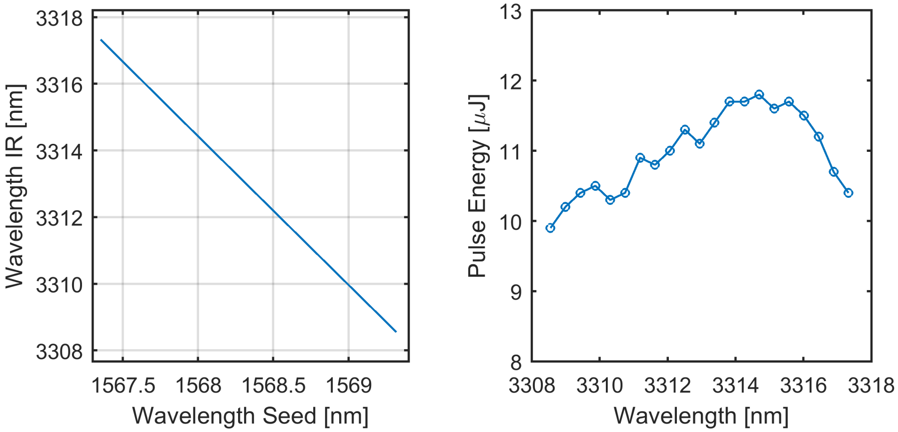

(a) The relationship between the seed laser wavelength and the generated mid-IR wavelength.

(b) Pulse energy as a function of wavelength. This was measured with a pump energy of 140µJ.

Figure 7.7

by recording an absorption spectrum, as described in Chapter 3. The results are shown in Figure 7.8. The gas cell was filled with 1% methane in N_2, at 50 mbar of pressure. The concentration was chosen to provide a clear, but non-saturating signal, and the pressure was chosen to narrow the linewidth of the transition lines enough that the broadening effect of the convolution with the laser lineshape was significant. The lineshape was assumed to be Gaussian, and by deconvolution the linewidth was found to be 0.0085 cm^{-1}.

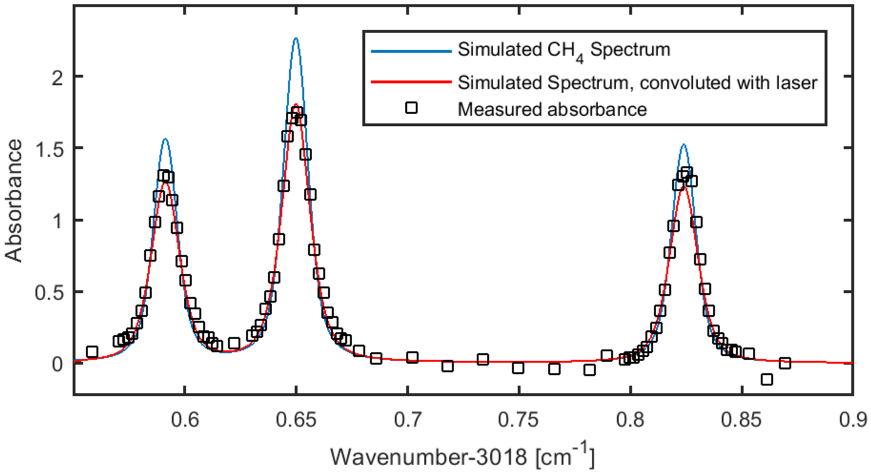

Figure 7.8: Absorption measurements where performed in a 40 cm long gas cell containing 1% CH_4 in N_2 at 50 mbar. By fitting a convolution of the calculated spectrum with a Gaussian laser line the linewidth was determined to be 0.0085 cm^{-1} (FWHM).

7.4.4 Outlook

The good pulse stability, continuous tuning and narrow linewidth makes this a promising basis for an alternative to the dye laser system. Attempts were made, unsuccesfully, to amplify the generated mid-IR pulses, but this might have been because the seeding system in the pump laser was malfunctioning during the work with implementing an amplification stage. Further work should focus on implementing an amplification stage, as pulse energies in the mJ range is required for generating DFWM and IRPS signals. It was found that the beamwaist in the generation stage was limited by the power of the seeding laser. If the beam waist was increased beyond the 70 µm used here, which would allow the use of higher pump energies, the seeding ceased to be effective. A higher power seed laser could therefore be one road to improved pulse energy output. The question is whether the good pulse stability can be maintained, or at least not degrade significantly, through amplification.

Chapter 8

Summary and Perspective

The overall aim of this thesis project was to improve the capabilities of nonlinear infrared spectroscopic techniques by adding upconversion detection. This aim was set on the basis of the promising results shown for DFWM in [105], where the upconversion detector achieved a 500 times higher signal-to-noise ratio, than the InSb detector used so far. In Paper II, a similar comparison was done using IRPS, which showed a factor 64 improvement in the signal-to-noise ratio. With upconversion, the new factor limiting the detection of weak signal for DFWM is background noise from light scattered from the pump and probe beam. For polarization spectroscopy the new limiting factor is the extinction ratio of the polarizer set used to block the probe beam. Having compared the sensitivity of the two methods, DFWM was chosen to detect HCN emitted from degassing straw pellets in Paper III. This was, as far as I am aware, the first demonstration of quantitative spatially and temporally resolved measurements of HCN in flames, and these measurements would not have been possible without the added sensitivity of the upconversion detector.

The main issue facing future work with quantitative detection of minor species, using the method described in Paper III, is accuracy, and the key to this will be improving the accuracy and precision of the temperature measurements. We have, in part, begun this with the investigation of the effect of line saturation on the waterline ratio, but there are still reliability issues to be solved, especially for the online detection method. In addition, the saturation measurements presented in this thesis only cover the 1500-1800 K range, and it would be highly advisable to perform a similar investigation of the 1000-1500 K range, before using the waterline ratio for temperature measurements in this range.

Expanding the success with HCN detection to other species is mainly limited by the availability of strong transition lines that do not overlap with transition lines from other molecular species, within the tuning range of the laser and the wavelength range of the detector. Ammonia has previously been detected in hot gas flows with DFWM, using lines near 2.3 µm. The sensitivity could be increased by the use of upconversion, but the PPLN crystal we have does not phase-match in this range. If funding for an additional PPLN crystal with a different set of poling periods could be obtained, allowing phase-match near 2.3 µm, NH_3 detection would be a worthwhile project.

8.1 Main results of the research papers

Paper i

Mid-Infrared Polarization Spectroscopy Measurements of Species Concentrations and Temperature in a Low Pressure Flame

In this paper, we demonstrated quantitative measurements of methane in a low pressure dimethyl ether/oxygen/argon flame using mid-infrared polarization spectroscopy. The quantification is achieved by calibrating the signal with a known concentration at room temperature and pressure, and combining this with calibration measurements of the pressure and temperature change response. In addition, the effect of different buffer gasses: Ar, N_2, and CO_2, on the signal strength were studied.

Paper ii

Comparison of an InSb Detector and an Upconversion Detector for Infrared Polarization Spectroscopy

A mid-infrared polarization spectroscopy signal was generated from a gas flow of methane in nitrogen, at room temperature and pressure. This signal was measured using an InSb detector and the upconversion detector to compare their signal-to-noise ratios. The upconversion detector achieved a signal-to-noise ratio 64 times higher than the InSb detector, which yields a detection limit a factor 8 lower.

Paper iii

Spatially and temporally resolved IR-DFWM measurement of HCN released from gasification of biomass pellets

Infrared degenerate four-wave mixing combined with upconversion detection was used to measure the release of HCN from strawpellets during gasification. The results were quantified by using calibration measurements done with known concentrations at room temperature, and extrapolating these to flame temperatures. The temperatures needed for this extrapolation were measured using waterline thermometry.

Paper iv

Infrared Degenerate Four-wave Mixing with Upconversion Detection for Quantitative Gas Sensing

In this video article, we presented the alignment procedure used for preparing the degenerate four wave mixing with upconversion detection. The focus here is purely on the method used in Paper III, and does not include new results.

Paper v

Characterization of the NEP of Mid-Infrared Upconversion Detectors

The noise equivalent power (NEP) of the upconversion detector for this thesis work is measured for different wavelength and temperatures and compared with theoretical calculations. In addition, this is compared with the NEP of other mid-infrared detectors and of other upconversion systems.

8.2 References

[1] Wubin Weng, Jesper Borggren, Bo Li, Marcus Aldén, and Zhongshan Li. A novel multi-jet burner for hot flue gases of wide range of temperatures and compositions for optical diagnostics of solid fuels gasification/combustion. *The Review Of Scientific Instruments*, 88(4):045104, 2017.

[2] L. S. Rothman et al. The HITRAN molecular spectroscopic database and

HAWKS (HITRAN Atmospheric WorKStation): 1996 edition. *Journal of Quantitative Spectroscopy and Radiative Transfer*, 60(5):665, 1998.

[3] L.S. Rothman, D. Jacquemart, A. Barbe, D. Chris Benner, M. Birk, L.R. Brown, M.R. Carleer, C. Chackerian, K. Chance, L.H. Coudert, V. Dana, V.M. Devi, J.-M. Flaud, R.R. Gamache, A. Goldman, J.-M. Hartmann, K.W. Jucks, A.G. Maki, J.-Y. Mandin, S.T. Massie, J. Orphal, A. Perrin, C.P. Rinsland, M.A.H. Smith, J. Tennyson, R.N. Tolchenov, R.A. Toth, J. Vander Auwera, P. Varanasi, and G. Wagner. The HITRAN 2004 molecular spectroscopic database. *Journal of Quantitative Spectroscopy and Radiative Transfer*, 96(2):139 – 204, 2005.

[4] I.E. Gordon, L.S. Rothman, C. Hill, R.V. Kochanov, Y. Tan, P.F. Bernath, M. Birk, V. Boudon, A. Campargue, K.V. Chance, B.J. Drouin, J.-M. Flaud, R.R. Gamache, J.T. Hodges, D. Jacquemart, V.I. Perevalov, A. Perrin, K.P. Shine, M.-A.H. Smith, J. Tennyson, G.C. Toon, H. Tran, V.G. Tyuterev, A. Barbe, A.G. Császár, V.M. Devi, T. Furtenbacher, J.J. Harrison, J.-M. Hartmann, A. Jolly, T.J. Johnson, T. Karman, I. Kleiner, A.A. Kyuberis, J. Loos, O.M. Lyulin, S.T. Massie, S.N. Mikhailenko, N. Moazzen-Ahmadi, H.S.P. Müller, O.V. Naumenko, A.V. Nikitin, O.L. Polyansky, M. Rey, M. Rotger, S.W. Sharpe, K. Sung, E. Starikova, S.A. Tashkun, J. Vander Auwera, G. Wagner, J. Wilzewski, P. Wcisło, S. Yu, and E.J. Zak. The HITRAN2016 molecular spectroscopic database. *Journal of Quantitative Spectroscopy and Radiative Transfer*, 203(HITRAN2016 Special Issue):3 – 69, 2017.

[5] R.V. Kochanov, I.E. Gordon, L.S. Rothman, P. Wcisło, C. Hill, and J.S. Wilzewski. HITRAN Application Programming Interface (HAPI): A comprehensive approach to working with spectroscopic data. *Journal of Quantitative Spectroscopy and Radiative Transfer*, 177(XVIIIth Symposium on High Resolution Molecular Spectroscopy (HighRus-2015), Tomsk, Russia):15 – 30, 2016.

[6] *HITRAN HAWKS and HITEMP: high-temperature molecular database*, volume 2471, 1995.

[7] L.S. Rothman, I.E. Gordon, R.J. Barber, H. Dothe, R.R. Gamache, A. Goldman, V.I. Perevalov, S.A. Tashkun, and J. Tennyson. HITEMP, the high-temperature molecular spectroscopic database. *Journal of Quantitative Spectroscopy and Radiative Transfer*, 111(15):2139 – 2150, 2010. XVIth Symposium on High Resolution Molecular Spectroscopy (HighRus-2009).

[8] Christopher S. Goldenstein, Victor A. Miller, R. Mitchell Spearrin, and Christopher L. Strand. Spectraplot.com: Integrated spectroscopic modeling of atomic and molecular gases. *Journal of Quantitative Spectroscopy and Radiative Transfer*, 200:249 – 257, 2017.

[9] B.E.A. Saleh & M.C. Teich. *Fundamentals of Photonics.* John Wiley & Sons, 2007.

[10] Richard L. Sutherland. *Handbook of Nonlinear Optics.* MarcelDekker,Inc, 2003.

[11] G. D. Boyd and D. A. Kleinman. Parametric interaction of focused gaussian light beams. *Journal of Applied Physics*, 39(8):3597–3639, 1968.

[12] Christian Pedersen, Qi Hu, Lasse Høgstedt, Peter Tidemand-Lichtenberg, and Jeppe Seidelin Dam. Non-collinear upconversion of infrared light. *Opt. Express*, 22(23):28027–28036, Nov 2014.

[13] C. Wieman and T. W. Hänsch. Doppler-free laser polarization spectroscopy. *Phys. Rev. Lett.*, 36:1170–1173, May 1976.

[14] Wolfgang E. Ernst. Doppler-free polarization spectroscopy of diatomic molecules in flame reactions. *Optics Communications*, 44(3):159 – 164, 1983.

[15] G. Zizak, J. Lanauze, and J. D. Winefordner. Cross-beam polarization in flames with a pulsed dye laser. *Appl. Opt.*, 25(18):3242–3246, Sep 1986.

[16] K. Nyholm, R. Maier, C. G. Aminoff, and M. Kaivola. Detection of OH in flames by using polarization spectroscopy. *Appl. Opt.*, 32(6):919–924, Feb 1993.

[17] K. Nyholm, R. Fritzon, and M. Aldén. Two-dimensional imaging of OH in flames by use of polarization spectroscopy. *Opt. Lett.*, 18(19):1672–1674, Oct 1993.

[18] Kaj Nyholm, Rolf Fritzon, Nikola Georgiev, and Marcus Aldén. Two-photon induced polarization spectroscopy applied to the detection of NH_3 and CO molecules in cold flows and flames. *Optics Communications*, 114(1):76 – 82, 1995.

[19] K. Nyholm, M. Kaivola, and C. G. Aminoff. Polarization spectroscopy applied to C_2 detection in a flame. *Applied Physics B*, 60(1):5–10, Jan 1995.

[20] S. Roy, R.P. Lucht, and A. McIlroy. Mid-infrared polarization spectroscopy of carbon dioxide. *Applied Physics B: Lasers and Optics*, 75(8):875–882, 2002.

[21] Z.T. Alwahabi, Z.S. Li, J. Zetterberg, and M. Aldén. Infrared polarization spectroscopy of CO_2 at atmospheric pressure. *Optics Communications*, 233(4):373 – 381, 2004.

[22] Z. T. Alwahabi, J. Zetterberg, Z. S. Li, and M. Aldén. High resolution polarization spectroscopy and laser induced fluorescence of CO_2 around 2µm. *European Physical Journal D – Atoms, Molecules, Clusters & Optical Physics*, 42(1):41 – 47, 2007.

[23] Z.S. Li, M. Rupinski, J. Zetterberg, and M. Aldén. Mid-infrared PS and LIF detection of CH_4 and C_2H_6 in cold flows and flames at atmospheric pressure. *Proceedings of the Combustion Institute*, 30(1):1629 – 1636, 2005.

[24] Z. S. Li, M. Rupinski, J. Zetterberg, Z. T. Alwahabi, and M. Aldén. Detection of methane with mid-infrared polarization spectroscopy. *Applied Physics B: Lasers & Optics*, 79(2):135 – 138, 2004.

[25] Z.S. Li, M. Linvin, J. Zetterberg, J. Kiefer, and M. Aldén. Mid-infrared polarization spectroscopy of C_2H_2: Non-intrusive spatial-resolved measurements of polyatomic hydrocarbon molecules for combustion diagnostics. *Proceedings of the Combustion Institute*, 31(1):817 – 824, 2007.

[26] Z. Sun, Z. Li, B. Li, Z.T. Alwahabi, and M. Aldén. Quantitative C_2H_2 measurements in sooty flames using mid-infrared polarization spectroscopy. *Applied Physics B-Lasers And Optics*, 101(1-2):423, 2010.

[27] Z.W. Sun, Z.S. Li, A.A. Konnov, and M. Aldén. Quantitative HCN measurements in $CH_4/N_2O/O_2/N_2$ flames using mid-infrared polarization spectroscopy. *Combustion & Flame*, 158(10):1898 – 1904, 2011.

[28] Z. S. Li, Changhong Hu, J. Zetterberg, M. Linvin, and M. Aldén. Midinfrared polarization spectroscopy of OH and hot water in low pressure lean premixed flames. *The Journal of Chemical Physics*, 127(8):084310, 2007.

[29] Zhiwei Sun, Johan Zetterberg, Zeyad Alwahabi, Marcus Aldén, and Zhongshan Li. Single-shot, planar infrared imaging in flames using polarization spectroscopy. *Opt. Express*, 23(23):30414–30420, Nov 2015.

[30] Wolfgang Demtröder. *Laser Spectroscopy 2*. Springer, 5th edition, 2015.

[31] Zhiwei Sun. *Development and application of non-linear mid-infrared laser spectroscopy for combustion diagnostics.* Lund reports on combustion physics: 159. Division of Combustion Physics, Department of Physics, Lund University, 2012.

[32] Johannes Kiefer and Paul Ewart. Laser diagnostics and minor species detection in combustion using resonant four-wave mixing. *Progress in Energy and Combustion Science*, 37(5):525 – 564, 2011.

[33] R. E. Teets, F. V. Kowalski, W. T. Hill, N. Carlson, and T. W. Hansch. Laser polarization spectroscopy. *Advances in Laser Spectrocopy I, SPIE Proceedings, San Diego*, 0113:80–87, 1977.

[34] Thomas A. Reichardt and Robert P. Lucht. Theoretical calculation of line shapes and saturation effects in polarization spectroscopy. *Journal of Chemical Physics*, 109(14):5830, 1998.

[35] Thomas A. Reichardt, William C. Giancola, and Robert P. Lucht. Experimental investigation of saturated polarization spectroscopy for quantitative concentration measurements. *Applied Optics*, 39(12):2002, 2000.

[36] R. L. Abrams and R. C. Lind. Degenerate four-wave mixing in absorbing media. *Opt. Lett.*, 2(4):94–96, Apr 1978.

[37] R. L. Abrams and R. C. Lind. Degenerate four-wave mixing in absorbing media: errata. *Opt. Lett.*, 3(5):205–205, Nov 1978.

[38] Thomas A. Reichardt, William C. Giancola, Christopher M. Shappert, and Robert P. Lucht. Experimental investigation of saturated degenerate four-wave mixing for quantitative concentration measurements. *Appl. Opt.*, 38(33):6951–6961, Nov 1999.

[39] R. T. Bratfalean, G. M. Lloyd, and P. Ewart. Degenerate four-wave mixing for arbitrary pump and probe intensities. *Journal of the Optical Society of America B: Optical Physics*, 16(6):952, 1999.

[40] Thomas A. Reichardt and Robert P. Lucht. Resonant degenerate four-wave mixing spectroscopy of transitions with degenerate energy levels: Saturation and polarization effects. *The Journal of Chemical Physics*, 111(22):10008–10020, 1999.

[41] S. M. Wandzura. Effects of atomic motion on wavefront conjugation by resonantly enhanced degenerate four-wave mixing. *Opt. Lett.*, 4(7):208–210, Jul 1979.

[42] Thomas A. Reichardt and Robert P. Lucht. Interaction of closely spaced resonances in degenerate four-wave-mixing spectroscopy. *J. Opt. Soc. Am. B*, 14(10):2449–2458, Oct 1997.

[43] Thomas A. Reichardt and Robert P. Lucht. Effect of doppler broadening on quantitative concentration measurements with degenerate four-wave mixing spectroscopy. *J. Opt. Soc. Am. B*, 13(6):1107–1119, Jun 1996.

[44] K. Bultitude, R. Bratfalean, and P. Ewart. Saturation effects in molecular spectroscopy using degenerate four-wave mixing. *Journal of Raman Spectroscopy*, 34(12):1030, 2003.

[45] Thomas A. Reichardt, Robert P. Lucht, Paul M. Danehy, and Roger L. Farrow. Theoretical investigation of the forward phase-matched geometry for degenerate four-wave mixing spectroscopy. *J. Opt. Soc. Am. B*, 15(10):2566–2572, Oct 1998.

[46] John Pender and Lambertus Hesselink. Phase conjugation in a flame. *Opt. Lett.*, 10(6):264–266, Jun 1985.

[47] P. Ewart and S. V. O'Leary. Detection of oh in a flame by degenerate four-wave mixing. *Opt. Lett.*, 11(5):279–281, May 1986.

[48] H. Bervas, B. Attal-Trétout, L. Labrunie, and S. Le Boiteux. Four-wave mixing in OH: comparison between CARS and DFWM. *Il Nuovo Cimento D*, 14(10):1043–1050, Oct 1992.

[49] Thomas Dreier and David J. Rakestraw. Degenerate four-wave mixing diagnostics on OH and NH radicals in flames. *Applied Physics B*, 50(6):479–485, Jun 1990.

[50] K. Nyholm. Two-dimensional imaging of oh in a flame by using degenerate four-wave mixing in a forward geometry. *Applied Physics B: Lasers & Optics*, 64(6):707, 1997.

[51] J. Tobai and T. Dreier. Measurement of relaxation times of nh in atmospheric pressure flames using picosecond pump-probe degenerate four-wave mixing. *Journal of Molecular Structure*, 480-481:307 – 310, 1999.

[52] A.J. Grant, P. Ewart, and C.R. Stone. Detection of NO in a spark-ignition research engine using degenerate four-wave mixing. *Applied Physics B: Lasers & Optics*, 74(1):105, 2002.

[53] N. Georgiev and M. Aldén. Two-photon degenerate four-wave mixing (DFWM) for the detection of ammonia: Applications to flames. *Applied Physics B*, 56(5):281–286, May 1993.

[54] P. Ewart and M. Kaczmarek. Two-dimensional mapping of temperature in a flame by degenerate four-wave mixing in OH. *Appl. Opt.*, 30(27):3996–3999, Sep 1991.

[55] B. Yip, P. M. Danehy, and R. K. Hanson. Degenerate four-wave mixing temperature measurements in a flame. *Opt. Lett.*, 17(10):751–753, May 1992.

[56] G.M. Lloyd, I.G. Hughes, R. Bratfalean, and P. Ewart. Broadband degenerate four-wave mixing of OH for flame thermometry. *Applied Physics B: Lasers & Optics*, 67(1):107, 1998.

[57] Geoffrey J. Germann, Roger L. Farrow, and David J. Rakestraw. Infrared degenerate four-wave mixing spectroscopy of polyatomic molecules: CH_4 and C_2H_2. *J. Opt. Soc. Am. B*, 12(1):25–32, Jan 1995.

[58] D. Voelkel, Yu.L. Chuzavkov, J. Marquez, S.N. Orlov, Yu.N. Polivanov, V.V. Smirnov, and F. Huisken. Infrared degenerate four-wave mixing and resonance-enhanced stimulated raman scattering in molecular gases and free jets. *Applied Physics B: Lasers & Optics*, 65(1):93, 1997.

[59] Anna-Lena Sahlberg, Jianfeng Zhou, Marcus Aldén, and Zhongshan Li. Investigation of ro-vibrational spectra of small hydrocarbons at elevated temperatures using infrared degenerate four-wave mixing. *Journal of Raman Spectroscopy*, 47(9):1130 – 1139, 2016.

[60] Y. Tang and S.A. Reid. Infrared degenerate four wave mixing spectroscopy of jet-cooled C_2H_2. *Chemical Physics Letters*, 248(5):476 – 481, 1996.

[61] Zhiwei Sun, Zhongshan Li, Bo Li, Marcus Aldén, and P. Ewart. Detection of C_2H_2 and HCl using mid-infrared degenerate four-wave mixing with stable beam alignment: towards practical in situ sensing of trace molecular species. *Applied Physics B: Lasers and Optics*, 98(2-3):593, 2010.

[62] J. Zhou, A. Sahlberg, H. Nilsson, E. Lundgren, and J. Zetterberg. Non-intrusive detection of methanol in gas phase using infrared degenerate four-wave mixing. *Applied Physics B: Lasers & Optics*, 121(2):123 – 130, 2015.

[63] A.-L. Sahlberg, J. Zhou, M. Aldén, and Z.S. Li. Non-intrusive in situ detection of methyl chloride in hot gas flows using infrared degenerate four-wave mixing. *Journal of Raman Spectroscopy*, 46(8):695–701, 2015.

[64] R.L. Vander Wal, B.E. Holmes, J.B. Jeffries, P.M. Danehy, R.L. Farrow, and D.J. Rakestraw. Detection of HF using infrared degenerate four-wave mixing. *Chemical Physics Letters*, 191(3):251 – 258, 1992.

[65] Geoffrey J. Germann and David J. Rakestraw. Multiplex spectroscopy: Determining the transition moments and absolute concentrations of molecular species. *Science*, 264(5166):1750–1753, 1994.

[66] A.-L. Sahlberg, D. Hot, M. Aldén, and Z.S. Li. Non-intrusive, in situ detection of ammonia in hot gas flows with mid-infrared degenerate four-wave mixing at 2.3 μm. *Journal of Raman Spectroscopy*, 47(9):1140–1148, 2016.

[67] Alan C. Eckbreth. *Laser diagnostics for combustion temperature and species.* Combustion science and technology book series: 3. Gordon & Breach, 1996.

[68] P. M. Danehy, E. J. Friedman-Hill, R. P. Lucht, and R. L. Farrow. The effects of collisional quenching on degenerate four-wave mixing. *Applied Physics B*, 57(4):243–248, Oct 1993.

[69] Roger L. Farrow, Thomas Dreier, and David J. Rakestraw. Investigation of the dependence of degenerate four-wave mixing line intensities on transition dipole moment. *Journal of the Optical Society of America B: Optical Physics*, 9(10):1770, 1992.

[70] G.M. Lloyd and P. Ewart. High resolution spectroscopy and spectral simulation of C_2 using degenerate four-wave mixing. *Journal of Chemical Physics*, 110(1):385, 1999.

[71] Anna-Lena Sahlberg. Non-linear mid-infrared laser techniques for combustion diagnostics. Master's thesis, Division of Combustion Physics, Department of Physics, Lund University, 2016.

[72] Sean P. Kearney, Kraig Frederickson, and Thomas W. Grasser. Dual-pump coherent anti-stokes raman scattering thermometry in a sooting turbulent pool fire. *Proceedings of the Combustion Institute*, 32(1):871 – 878, 2009.

[73] Sukesh Roy, James R. Gord, and Anil K. Patnaik. Recent advances in coherent anti-stokes raman scattering spectroscopy: Fundamental developments and applications in reacting flows. *Progress in Energy and Combustion Science*, 36(2):280 – 306, 2010.

[74] Michael P. Lee, Brian K. McMillin, and Ronald K. Hanson. Temperature measurements in gases by use of planar laser-inducedfluorescence imaging of NO. *Appl. Opt.*, 32(27):5379–5396, Sep 1993.

[75] A.T. Hartlieb, B. Atakan, and K. Kohse-Höinghaus. Temperature measurement in fuel-rich non-sooting low-pressure hydrocarbon flames. *Applied Physics B*, 70(3):435–445, Mar 2000.

[76] Jesper Borggren, Iain S. Burns, Anna-Lena Sahlberg, Marcus Aldén, and Zhongshan Li. Temperature imaging in low-pressure flames using diode laser two-line atomic fluorescence employing a novel indium seeding technique. *Applied Physics B*, 122(3):58, Mar 2016.

[77] I. S. Burns, N. Lamoureux, C. F. Kaminski, J. Hult, and P. Desgroux. Diode laser atomic fluorescence temperature measurements in low-pressure flames. *Applied Physics B: Lasers & Optics*, 93(4):907 – 914, 2008.

[78] Ben Williams, Megan Edwards, Richard Stone, John Williams, and Paul Ewart. High precision in-cylinder gas thermometry using laser induced gratings: Quantitative measurement of evaporative cooling with gasoline/alcohol blends in a GDI optical engine. *Combustion and Flame*, 161(1):270 – 279, 2014.

[79] H. Latzel, A. Dreizler, T. Dreier, J. Heinze, M. Dillmann, W. Stricker, G.M. Lloyd, and P. Ewart. Thermal grating and broadband degenerate four-wave mixing spectroscopy of oh in high-pressure flames. *Applied Physics B: Lasers & Optics*, 67(5):667, 1998.

[80] Anna-Lena Sahlberg, Dina Hot, Johannes Kiefer, Marcus Aldén, and Zhongshan Li. Mid-infrared laser-induced thermal grating spectroscopy in flames. *Proceedings of the Combustion Institute*, 36(3):4515 – 4523, 2017.

[81] Z. W. Sun, Z. S. Li, B. Li, and M. Aldén. Flame temperature diagnostics with water lines using mid-infrared degenerate four-wave mixing. *Journal of Raman Spectroscopy*, 42(10):1828, 2011.

[82] D. A. Kleinman and G. D. Boyd. Infrared detection by optical mixing. *Journal of Applied Physics*, 40(2):546–566, 1969.

[83] J. S. Dam, P. Tidemand-Lichtenberg, and C. Pedersen. Room-temperature mid-infrared single-photon spectral imaging. *Nature Photonics*, 6(11):788 – 793, 2012.

[84] M. Hermes, R. Brandstrup Morrish, L. Huot, et al. Mid-IR hyperspectral imaging for label-free histopathology and cytology. *Journal of Optics*, 20(2):1, 2018.

[85] Ajanta Barh, Christian Pedersen, and Peter Tidemand-Lichtenberg. Ultra-broadband mid-wave-IR upconversion detection. *Opt. Lett.*, 42(8):1504–1507, Apr 2017.

[86] Louis Martinus Kehlet, Peter Tidemand-Lichtenberg, Jeppe Seidelin Dam, and Christian Pedersen. Infrared upconversion hyperspectral imaging. *Opt. Lett.*, 40(6):938–941, Mar 2015.

[87] Louis Martinus Kehlet, Nicolai Sanders, Peter Tidemand-Lichtenberg, Jeppe Seidelin Dam, and Christian Pedersen. Infrared hyperspectral upconversion imaging using spatial object translation. *Opt. Express*, 23(26):34023–34028, Dec 2015.

[88] Laurent Huot, Peter Morten Moselund, Peter Tidemand-Lichtenberg, Lasse Leick, and Christian Pedersen. Upconversion imaging using an all-fiber supercontinuum source. *Opt. Lett.*, 41(11):2466–2469, Jun 2016.

[89] Romain Demur, Renaud Garioud, Arnaud Grisard, Eric Lallier, Luc Leviandier, Loïc Morvan, Nicolas Treps, and Claude Fabre. Near-infrared to visible upconversion imaging using a broadband pump laser. *Opt. Express*, 26(10):13252–13263, May 2018.

[90] S. Junaid, S. Chaitanya Kumar, M. Mathez, M. Hermes, N. Stone, N. Shepherd, M. Ebrahim-Zadeh, P. Tidemand-Lichtenberg, and C. Pedersen. Video-rate, mid-infrared hyperspectral upconversion imaging. *Optica*, 6(6):702–708, Jun 2019.

[91] Saher Junaid, Jan Tomko, Mykhaylo P. Semtsiv, Jan Kischkat, W. Ted Masselink, Christian Pedersen, and Peter Tidemand-Lichtenberg. Mid-infrared upconversion based hyperspectral imaging. *Opt. Express*, 26(3):2203–2211, Feb 2018.

[92] Yu-Pei Tseng, Christian Pedersen, and Peter Tidemand-Lichtenberg. Upconversion detection of long-wave infrared radiation from a quantum cascade laser. *Opt. Mater. Express*, 8(5):1313–1321, May 2018.

[93] Yu-Pei Tseng, Pascaline Bouzy, Christian Pedersen, Nick Stone, and Peter Tidemand-Lichtenberg. Upconversion raster scanning microscope for long-wavelength infrared imaging of breast cancer microcalcifications. *Biomed. Opt. Express*, 9(10):4979–4987, Oct 2018.

[94] Lasse Høgstedt, Andreas Fix, Martin Wirth, Christian Pedersen, and Peter Tidemand-Lichtenberg. Upconversion-based lidar measurements of atmospheric CO_2. *Opt. Express*, 24(5):5152–5161, Mar 2016.

[95] Lichun Meng, Andreas Fix, Martin Wirth, Lasse Høgstedt, Peter Tidemand-Lichtenberg, Christian Pedersen, and Peter John Rodrigo. Upconversion detector for range-resolved DIAL measurement of atmospheric CH_4. *Opt. Express*, 26(4):3850–3860, Feb 2018.

[96] Sebastian Wolf, Tobias Trendle, Jens Kiessling, Johannes Herbst, Karsten Buse, and Frank Kühnemann. Self-gated mid-infrared short pulse upconversion detection for gas sensing. *Opt. Express*, 25(20):24459–24468, Oct 2017.

[97] Haiyun Xia, Guoliang Shentu, Mingjia Shangguan, Xiuxiu Xia, Xiaodong Jia, Chong Wang, Jun Zhang, Jason S. Pelc, M. M. Fejer, Qiang Zhang, Xiankang Dou, and Jian-Wei Pan. Long-range micro-pulse aerosol lidar at 1.5 μm with an upconversion single-photon detector. *Opt. Lett.*, 40(7):1579–1582, Apr 2015.

[98] Laurent Huot, Peter Morten Moselund, Peter Tidemand-Lichtenberg, and Christian Pedersen. Electronically delay-tuned upconversion cross-correlator for characterization of mid-infrared pulses. *Opt. Lett.*, 43(12):2881–2884, Jun 2018.

[99] Søren Roesgaard, Lichun Meng, Peter Tidemand-Lichtenberg, Jeppe Seidelin Dam, Peter John Rodrigo, Christian Pedersen, and Brian Julsgaard. Time-resolved infrared photoluminescence spectroscopy using parametric three-wave mixing with angle-tuned phase matching. *Opt. Lett.*, 43(12):3001–3004, Jun 2018.

[100] Morgan Mathez, Peter John Rodrigo, Peter Tidemand-Lichtenberg, and Christian Pedersen. Upconversion imaging using short-wave infrared picosecond pulses. *Opt. Lett.*, 42(3):579–582, Feb 2017.

[101] Ashik A. S., Callum F. O'Donnell, S. Chaitanya Kumar, M. Ebrahim-Zadeh, P. Tidemand-Lichtenberg, and C. Pedersen. Mid-infrared upconversion imaging using femtosecond pulses. *Photon. Res.*, 7(7):783–791, Jul 2019.

[102] Israelsen Niels M., Petersen Christian R., Barh Ajanta, Jain Deepak, Jensen Mikkel, Hannesschläger Günther, Tidemand-Lichtenberg Peter, Pedersen Christian, Podoleanu Adrian, and Bang Ole. Real-time high-resolution mid-infrared optical coherence tomography. *Light: Science & Applications*, 8(1):1, 2019.

[103] R. Tang, W. Wu, X. Li, H. Pan, H. Zeng, and E. Wu. Low-noise infrared spectroscopy via tunable frequency upconversion at single-photon level. *IEEE Photonics Technology Letters*, 27(15):1642–1645, Aug 2015.

[104] M Mancinelli, A Trenti, S Piccione, G Fontana, J S Dam, P Tidemand-Lichtenberg, C Pedersen, and L Pavesi. Mid-infrared coincidence measurements on twin photons at room temperature. *Nature Communications*, 8:15184, 2017.

[105] Lasse Høgstedt, Jeppe Seidelin Dam, Anna-Lena Sahlberg, Zhongshan Li, Marcus Alden, Christian Pedersen, and Peter Tidemand-Lichtenberg. Low-noise mid-IR upconversion detector for improved IR-degenerate four-wave mixing gas sensing. *Optics Letters*, 39(18):5321–5324, 2014.

[106] O. Gayer, Z. Sacks, E. Galun, and A. Arie. Temperature and wavelength dependent refractive index equations for MgO-doped congruent and stoichiometric $\mathrm{LiNbO_3}$. *Applied Physics B: Lasers & Optics*, 91(2):343 – 348, 2008.

[107] Lichun Meng, Lasse Høgstedt, Peter Tidemand-Lichtenberg, Christian Pedersen, and Peter John Rodrigo. Enhancing the detectivity of an upconversion single-photon detector by spatial filtering of upconverted parametric fluorescence. *Optics Express*, 26(19):24712 – 24722, 2018.

[108] Ajanta Barh, Peter Tidemand-Lichtenberg, and Christian Pedersen. Thermal noise in mid-infrared broadband upconversion detectors. *Optics Express*, 26(3):3249 – 3259, 2018.

[109] Qi Hu, Jeppe Seidelin Dam, Christian Pedersen, and Peter Tidemand-Lichtenberg. High-resolution mid-IR spectrometer based on frequency upconversion. *Optics Letters*, 37(24):5232 – 5234, 2012.

[110] Gu Xiaorong, Huang Kun, Pan Haifeng, Wu E., and Zeng Heping. Efficient mid-infrared single-photon frequency upconversion detection with ultralow background counts. *Laser Physics Letters*, 10(5):1, 2013.

[111] Carsten Langrock, Eleni Diamanti, Rostislav V. Roussev, Yoshihisa Yamamoto, M. M. Fejer, and Hiroki Takesue. Highly efficient single-photon detection at communication wavelengths by use of upconversion in reverse-proton-exchanged periodically poled LiNbO3 waveguides. *Opt. Lett.*, 30(13):1725–1727, Jul 2005.

[112] Paul L. Voss, Kahraman G. Köprülü, Sang-Kyung Choi, Sarah Dugan, and Prem Kumar. 14 MHz rate photon counting with room temperat-

ure InGaAs/InP avalanche photodiodes. *Journal of Modern Optics*, 51(9-10):1369–1379, 2004.

[113] J. S. Pelc, C. Langrock, Q. Zhang, and M. M. Fejer. Influence of domain disorder on parametric noise in quasi-phase-matched quantum frequency converters. *Optics letters*, 35(16):2804–2806, 2010.

[114] U. Bäder, T. Mattern, T. Bauer, J. Bartschke, M. Rahm, A. Borsutzky, and R. Wallenstein. Pulsed nanosecond optical parametric generator based on periodically poled lithium niobate. *Optics Communications*, 217(1):375 – 380, 2003.

[115] C. Fischer and M.W. Sigrist. Trace-gas sensing in the 3.3-µm region using a diode-based difference-frequency laser photoacoustic system. *Applied Physics B: Lasers & Optics*, 75(2/3):305, 2002.

[116] Sebastian Wolf, Tobias Trendle, Jens Kiessling, Johannes Herbst, Karsten Buse, and Frank Kühnemann. Self-gated mid-infrared short pulse upconversion detection for gas sensing. *Opt. Express*, 25(20):24459–24468, Oct 2017.

[117] L Liu, H Y Wang, Y Ning, C Shen, L Si, Y Yang, Q L Bao, and G Ren. Sub-nanosecond periodically poled lithium niobate optical parametric generator and amplifier pumped by an actively Q-switched diode-pumped Nd:YAG microlaser. *Laser Physics*, 27(5):055403, mar 2017.

[118] Thomas A. Reichardt, Ray P. Bambha, Thomas J. Kulp, and Randal L. Schmitt. Frequency-locked, injection-seeded, pulsed narrowband optical parametric generator. *Appl. Opt.*, 42(18):3564–3569, Jun 2003.

Scientific publications

Author contributions

Co-authors are abbreviated as follows:
Dina Hot (DH), Anna-Lena Sahlberg (AS), Zhongshan Li (ZL), Wubin Weng (WW), Yuhe Zhang (YZ), Jianfeng Zhou (JZ), Marcus Aldén (MA). Lasse Høgstedt (LH), Ajanta Barh (AB), Lichun Meng (LM), Rasmus Lyngbye Pedersen (RP), and Peter Tidemand-Lichtenberg (PTL)

Paper i: Mid-Infrared Polarization Spectroscopy Measurements of Species Concentrations and Temperature in a Low-Pressure Flame

Applied Spectroscopy, 2019, Vol. 73, p. 1–12
Authors: AS, DH, RP, JZ, MA, and ZL.
I took part in the lab work, the final proof-reading and editing, and addressed some of the reviewer comments. AS and DH were responsible for the bulk of the labwork and writing. MA and ZL assisted in the writing and proof-reading of the article.

Paper ii: Comparison of an InSb Detector and Upconversion Detector for Infrared Polarization Spectroscopy

Applied Spectroscopy, 2018, Vol. 72, p. 793–797
Authors: RP, DH, and ZL.
I planned and executed the labwork and wrote the article. DH helped with the labwork and writing. ZL assisted with writing and proofreading.

Paper iii: Spatially and temporally resolved IR-DFWM measurement of HCN released from gasification of biomass pellets

Proceedings of the Combustion Institute, 2019, Vol. 37, p. 1337–1344
Authors: DH, RP, WW, YZ, MA, and ZL.
I was responsible for upconversion detector during the labwork and for most of the data analysis afterwards. I wrote the description of the upconversion detector and a large part of the results and discussion section. DH was responsible mainly for the IR-laser and signal generation part of the setup. DH was also the main author coordinating the different subsections of the article. WW was responsible for the multijet burner and fuel, as well as the parts of the article that relates to that. YZ assisted with various tasks in the lab, and made Figure 2. All authors assisted with the proof-reading and editing of the final article.

Paper iv: Infrared Degenerate Four-wave Mixing with Upconversion Detection for Quantitative Gas Sensing

Journal of Visualized Experiments, 2019, p. 1–7
Authors: RP, ZL.
I was responsible for the labwork done, and for writing the article. ZL assisted with proof-reading.

Paper v: Characterization of the NEP of Mid-Infrared Upconversion Detectors

IEEE PHOTONICS TECHNOLOGY LETTERS, 2019, Vol. 31, p. 681–684
Authors: RP, LH, AB, LM, and PTL.
I was responsible for the labwork and the data analysis. AB was responsible for thermal noise theory. LM was responsible for the USPDC-noise theory. LH prepared the necessary equipment for the labwork, and assisted with part of labwork. All authors took part in editing and proof-reading the article.